REPORT DOCUMENTATION PAGE

Form Approved OMB NO. 0704-0188

1. REPORT DATE (DD-MM-YYYY)	2. REPORT TYPE	3. DATES COVERED (From - To)
31-08-2023	Thesis or Dissertation	-

4. TITLE AND SUBTITLE
Circuit QED in the ultrastrong coupling regime under incoherent excitations

5a. CONTRACT NUMBER
W911NF-19-1-0065

5b. GRANT NUMBER

5c. PROGRAM ELEMENT NUMBER
611102

6. AUTHORS
Samuel, Napoli

5d. PROJECT NUMBER

5e. TASK NUMBER

5f. WORK UNIT NUMBER

7. PERFORMING ORGANIZATION NAMES AND ADDRESSES
Universita di Messina
Piazza Pugliatti, 1
Viale Stagno D'Alcontres 31
00000 -

8. PERFORMING ORGANIZATION REPORT NUMBER

9. SPONSORING/MONITORING AGENCY NAME(S) AND ADDRESS (ES)
U.S. Army Research Office
P.O. Box 12211
Research Triangle Park, NC 27709-2211

10. SPONSOR/MONITOR'S ACRONYM(S)
ARO

11. SPONSOR/MONITOR'S REPORT NUMBER(S)
73511-EM-INT.27

12. DISTRIBUTION AVAILIBILITY STATEMENT

13. SUPPLEMENTARY NOTES
The views, opinions and/or findings contained in this report are those of the author(s) and should not contrued as an official Department of the Army position, policy or decision, unless so designated by other documentation.

14. ABSTRACT

15. SUBJECT TERMS

16. SECURITY CLASSIFICATION OF:			17. LIMITATION OF ABSTRACT	15. NUMBER OF PAGES	19a. NAME OF RESPONSIBLE PERSON
a. REPORT	b. ABSTRACT	c. THIS PAGE			Salvatore Savasta
					19b. TELEPHONE NUMBER +39-327-5432

REPORT DOCUMENTATION PAGE (SF298)
(Continuation Sheet)

Continuation for Block 13

Proposal/Report Number: 73511.27-EM-INT

Report Title: Circuit QED in the ultrastrong coupling regime under incoherent excitations
Report Type: Ph.D. Dissertation

Publication Type: Thesis or Dissertation
Institution: University of Messina
Date Received: 31-Aug-2023 Completion Date: 7/5/23 12:07PM
Title: Circuit QED in the ultrastrong coupling regime under incoherent excitations
Authors: Samuel, Napoli
Acknowledged Federal Support: **Y**

Università degli Studi di Messina
Department of Mathematical and Computer Sciences,
Physical Sciences and Earth Sciences

Master's Degree Thesis in Physics

Circuit QED in the ultrastrong coupling regime under incoherent excitations

Candidate:
Samuel Napoli

Supervisor:
Prof. Omar Di Stefano

Co-Supervisor:
Prof. Salvatore Savasta

Academic Year 2022/2023

Contents

List of Figures

Acknowledgements

I would like to thank my supervisor, Prof. Omar Di Stefano, and co-supervisor, Prof. Salvatore Savasta, for their support and availability. In addition, I am obliged to Dr. Alberto Mercurio for introducing me to the methods concerning computational quantum mechanics. Also, I am grateful to my old friend Davide Sgrò for helping me with the realization of the circuit diagrams. Finally, I would like to thank my parents, colleagues and friends for the moral support they provided.

Introduction

Nowadays many people are well aware of quantum computers and the enormous resources employed by leading companies, such as *Google inc.* and *IBM*, to develop this new technology. The quantum computers designed by these companies are based on superconducting quantum circuits. The building blocks are superconducting artificial atoms, also known as superconducting qubits. The research activity studying superconducting quantum circuits in interaction with microwave photons is known as circuit quantum electrodynamics (QED). This topic is the analogous of cavity QED for superconductive circuits. Cavity QED studies the interaction between atoms or collective excitations in solid state systems and photons in regimes where the nonclassical properties of the electromagnetic field emerge.

In the last decades, it has been understood that the principles of quantum mechanics hold the potential for significantly enhancing performance beyond the capabilities of classical systems. By leveraging the peculiarities of quantum phenomena, we can unlock new frontiers of efficiency, speed, and computational power that surpass the limits of classical frameworks [1]. Quantum computers represent probably the most important application of second-generation quantum technologies. They are merely the best known example of a whole series of conceivable innovative applications for putting quantum-mechanical effects to controlled use. Examples of interesting applications are the development of technologies enabling the design of tap-proof communication channels, novel simulation methods that might be used in materials development, development of quantum sensors that can outperform classical ones [2–5].

Cavity QED played a prominent pioneering role in the development of second-generation quantum technologies. The intricate interactions between light and matter in cavity QED determine drastically different behaviors

depending on the relative magnitude of the light-matter coupling. In the weak-coupling regime, the losses in the system exceed the light-matter coupling strength, and energy in the system is primarily lost before it has the chance to coherently transfer between the matter and the light. Accessing this regime experimentally has allowed for breakthroughs in quantum technologies such as single-photon emitters [6]. Going beyond weak-coupling, the strong-coupling regime is characterized by lower losses in the system, permitting the observation of vacuum Rabi oscillations: the coherent oscillatory exchange of energy between light and matter. The strong-coupling regime has helped initiate a second generation of quantum technologies [5]. Around 2005, the ultrastrong-coupling (USC) regime was predicted for intersubband polaritons [7]. This regime is characterized not by still lower losses, but by a coupling strength that is a comparable fraction of the bare energies of the system. The dimensionless parameter $\eta = g/\omega_0$ (i.e., the cavity-emitter coupling rate divided by the transition frequency) is used to quantify this coupling regime for cavity QED. Typically, USC effects are expected when $\eta \gtrsim 0.1$, at which point the rotating wave approximation (RWA) used in the weak and strong regimes becomes invalid. Reported signs of USC emerged in 2009 with experiments involving quantum-well intersubband microcavities [8], achieving $\eta \approx 0.11$. Terahertz-driven quantum wells have also demonstrated USC effects [9], and similar effects have been exploited to achieve carrier-wave Rabi flopping with strong optical pulses [10, 11]. To date, many different systems have exhibited USC [3]. With experiments pushing the normalized coupling strength continuously higher, the interest in USC also continues to grow, helping to improve the underlying theories of light-matter interactions.

In experiments with superconducting circuits [12], in which USC was observed for the first time in 2010, with $\eta = 0.10 - 0.12$ [13, 14], it becomes possible to explore the USC of light to a single two-level system (qubit), instead of a collective excitation. In contrast to natural atoms, superconducting artificial atoms can be designed, fabricated, and controlled for various research purposes. Furthermore, the interaction between artificial atoms and electromagnetic fields can be artificially engineered. Hence, SQCs can possess some features, which are very different from those of natural atoms. Circuit QED

is finding its application for the development of key elements for quantum information processing, such as the qubit readout. Moreover, it can be used to demonstrate phenomena that cannot be realized or observed in atomic physics and quantum optics. For instance, single- and two-photon processes can coexist in SQCs, and the coupling between them and microwave fields can become ultrastrong.

This work explores the emission of photons under incoherent excitations of the artificial atom in circuit QED systems in the USC regime [15–17]. Specifically, we study a circuit QED system out of thermal equilibrium, considering the qubit (a flux qubit artificial atom) coupled to a reservoir at an effective temperature T_q different from zero, and the electromagnetic resonator T_c such that $T_c << T_q$.

The thesis is structured as follows:

1. Chapter 1 has the purpose to introduce and describe the circuit QED system which is investigated in this thesis. In Sec. 1.1 fundamental theoretical tools will be introduced and analyzed. *Circuit quantization* is the starting point to tackle quantum superconductive circuits. Then, that procedure will be performed on the LC circuit.
   Sec. 1.2 will be dedicated to presenting a relevant artificial atom configuration, that is, the flux qubit. In addition, its quantization, operating principles, and approximations are the subjects of the treatment.
   Sec. 1.3 finalizes the description of the model showing the circuit configurations that establish the galvanic coupling between an LC resonator and a flux qubit. As a consequence of this theory, the choice of the *gauge* represents a delicate matter to discuss.

2. As mentioned above, interaction with the environment has to be considered. For this reason, the formalism of the *master equation* is the main topic of Chapter 2. When the ultrastrong coupling regime is reached, $\eta \geq 0.1$, the situation becomes more complex. At the beginning of chapter 2, several critical issues will be discussed.
   Sec. 2.1.1 concerns the derivation of a generalized master equation, which works properly in any light-matte coupling regime, following the

studies of [18, 19].
The dressed master equation, introduced in [20], provided a great insight into dissipation in the ultrastrong coupling, Sec. 2.1.2 covers this topic stressing the differences and the necessary conditions for its employment.
Sec. 2.2 offers a practical example of coupling with the environment, that is, the connection of the circuit with a transmission line via a mutual inductance, then through a capacitor.

3. Chapter 3 reports the numerical results. First, the idea is to show the energy eigenvalues of the LC-flux qubit Hamiltonian as functions of a few key parameters. Then, emission spectra will be presented and analyzed.

4. Appendix A shows most of the necessary computations to derive the *generalized master equation*.

5. Appendix B goes into detail about the methods referring to numerical simulation.

In summary, in this thesis work, studying the emission from a circuit QED system under incoherent qubit excitation, we show that capacitive and inductive coupling of the electromagnetic resonator with the transmission line used for the detection (output port) can give rise to significantly different emission spectra when the circuit QED system is in the USC and dispersive regime.

Chapter 1

Model description

In this chapter, we consider a single flux qubit circuit coupled to an LC oscillator. In particular, a theoretical description of the flux qubit and the LC oscillator is developed, and, afterward, an in-depth discussion about the type of coupling will be carried out.

1.1 LC resonator

A cavity represents a fundamental element in light-matter interaction experiments (Cavity QED) to achieve the most promising coupling regimes. Regarding the superconductive circuit QED applications, the counterparts of a cavity are various kinds of resonators, principally coplanar waveguides and LC oscillators. The latter is chosen to be coupled to a qubit because of undeniable advantages that are going to be clarified later on.

Dealing with superconductor circuits, which implies zero resistance value and dissipation effects, corresponds to determining the Lagrangian for an electric circuit composed of lumped elements whose characteristic length l is much less than the wavelength of typical microwave signals, therefore, measurable electric quantities can be assumed to be only time-dependent. A Lagrangian for a specific circuit can be derived following the procedures presented in Ref. [21, 22]. In summary, it is always possible to decompose a circuit by a ground node and a set of branches that are not redundant [22]. Generalized variables such as branch voltages v_b or branch currents i_b can be defined for each of them. Then, applying the Kirchoff rules, the node voltages v_n and the node currents i_n can be expressed as the sum of the

branch counterparts. Hence, kinetic energy and potential energy can be written as functions of the quantities

$$\Phi_n(t) = \int_{-\infty}^{t} v(\tau)d\tau\,, \tag{1.1}$$

$$Q_n = \int_{-\infty}^{t} i(\tau)d\tau\,, \tag{1.2}$$

where the former, Eq. (1.1), represents the node fluxes, and the latter, Eq. (1.2), represents the node charges. Ultimately, the Lagrangian and the Hamiltonian can be computed and the total dynamic will be determined. This method clearly suggests that there does not exist a single possible Lagrangian.

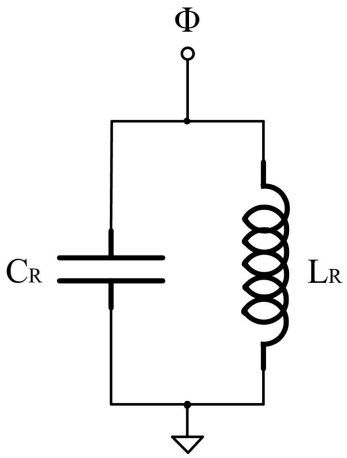

Figure 1.1: **LC resonator electric circuit**. The node flux Φ through the inductance is the generalized variable and the charge Q stored in the capacitor is the conjugate momentum.

Following this prescription for the LC circuit, which is visualized in Fig. 1.1, the procedure results in a rather trivial task. The energy stored in the capacitor $\frac{1}{2}C_r\dot{\Phi}^2$ is associated with the kinetic energy, while the potential energy is equal to the magnetic energy $\frac{1}{2L_r}\Phi^2$ in the inductor. Given

that choice of generalized coordinates, the Lagrangian is written as:

$$\mathcal{L} = \frac{1}{2} C_r \dot{\Phi}^2 - \frac{1}{2\,L_r} \Phi^2 \,; \tag{1.3}$$

that clearly shows the analogy with the harmonic oscillator.
The conjugate momentum to the Φ is obtained through:

$$\frac{\partial \mathcal{L}}{\partial \dot{\Phi}} = C_r \dot{\Phi} = Q \,, \tag{1.4}$$

where Q assumes the role of the charge in the capacitor.
If we are interested in moving from Lagrangian to Hamiltonian formalism, the following Legendre transformation has to be performed:

$$\mathcal{H} = Q\dot{\Phi} - \mathcal{L} = \frac{Q^2}{2C_r} + \frac{\Phi^2}{2L_r} \,. \tag{1.5}$$

The equation of motion can be trivially computed by means of Hamilton's equation:

$$\dot{\Phi} = \frac{\partial \mathcal{H}}{\partial Q} = \frac{Q}{C_r} \,, \tag{1.6}$$

and

$$\dot{Q} = -\frac{\partial \mathcal{H}}{\partial \Phi} = -\frac{\Phi}{L_r} \,. \tag{1.7}$$

To describe a quantum system, conjugate variables are promoted to quantum operators that satisfy the canonical commutation rule $[\hat{\Phi}, \hat{Q}] = i\hbar$. Now, it is common to proceed similarly to a quantum harmonic oscillator by defining the proper raising and lowering operators [23]:

$$\hat{a} = +i \frac{1}{\sqrt{2C_r\,\omega_r \hbar}}\,\hat{Q} + \frac{1}{\sqrt{2L_r\,\omega_r \hbar}}\,\hat{\Phi} \,; \tag{1.8}$$

$$\hat{a}^\dagger = -i \frac{1}{\sqrt{2C_r\,\omega_r \hbar}}\,\hat{Q} + \frac{1}{\sqrt{2L_r\,\omega_r \hbar}}\,\hat{\Phi} \,; \tag{1.9}$$

where $\omega_r = \dfrac{1}{\sqrt{L_r C_r}}$ is the frequency of the oscillator. Summing and subtracting Eq. (1.8) and Eq. (1.9), it is possible to express the charge and flux

operators as:

$$\hat{Q} = -iQ_{ZPF}\left(\hat{a} - \hat{a}^{\dagger}\right) , \tag{1.10}$$

$$\hat{\Phi} = \Phi_{ZPF}\left(\hat{a} + \hat{a}^{\dagger}\right) . \tag{1.11}$$

where $Q_{ZPF} = \sqrt{\frac{\hbar}{2Z}}$, $\Phi_{ZPF} = \sqrt{\frac{\hbar Z}{2}}$ are the zero-point charge and flux fluctuations, with $Z = \sqrt{\frac{L_r}{C_r}}$ the circuit impedance. Substituting Eq. (1.8) and Eq. (1.9) in Eq. (1.5), the typical harmonic oscillator Hamiltonian operator can be found:

$$\hat{\mathcal{H}} = \hbar\omega_r \left\{\hat{a}^{\dagger}\hat{a} + \frac{1}{2}\right\} . \tag{1.12}$$

Finally, a fundamental relation, which will be useful concerning the computation of spectra, has to be explained. Voltage operator can be obtained by relying on the Heisenberg picture and the commutation rules of raising and lowering operators:

$$\hat{V} = \frac{d\hat{\Phi}}{dt} = \frac{i}{\hbar}[\hat{\mathcal{H}}, \hat{\Phi}] = \frac{i}{\hbar}\hbar\omega_r\Phi_{ZPF}\left\{[\hat{a^{\dagger}}\hat{a}, \hat{a}] + [\hat{a^{\dagger}}\hat{a}, \hat{a^{\dagger}}]\right\} = -iV_{ZPF}(\hat{a} - \hat{a^{\dagger}}) . \tag{1.13}$$

where $V_{ZPF} = \omega_r \Phi_{ZPF}$. In summary, a superconducting LC circuit behaves like a harmonic oscillator whose quanta can be interpreted as photons. Tuning the values of the inductor or the capacitor, high zero-point current fluctuations can be easily attained, which represents a key factor in order to achieve stronger coupling regimes between artificial atoms and resonators, such as ultrastrong (USC) and deep strong coupling (DSC) [16]. Furthermore, the single-mode approximation is often a useful tool in cavity QED to simplify the system. This assumption is valid, without approximation, in an LC oscillator that has a single characteristic frequency; conversely, a cavity is composed of multiple modes separated in frequency.

1.2 Flux Qubit

Natural atoms exhibit an anharmonic spectrum, characterized by the fact that each transition between two energy levels is typically distinct from one another. On the contrary, as we have shown before, an LC circuit (harmonic oscillator) gives rise to an energy spectrum that is distinguished by evenly spaced levels, emerging from the quadratic potential energy (Eq. (1.5)). In order to simulate the peculiar spectra of real atoms, a nonlinear circuit component is needed (non-quadratic potential).

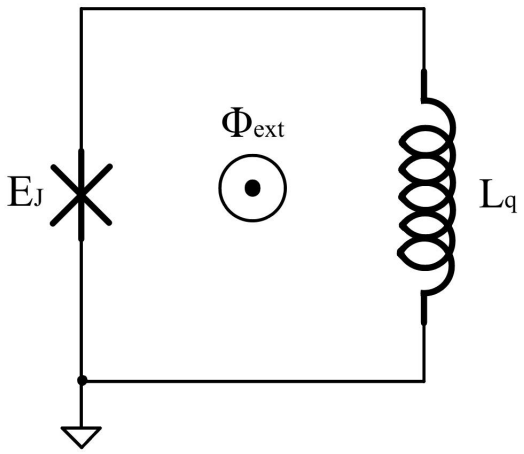

Figure 1.2: **Circuit representation of a flux qubit**. Josephson junction is indicated by the cross, L_q is due to the superconductive ring, and C_q is the junction capacitance that is implied.

Josephson tunnel junctions were a breakthrough regarding circuit QED; it consists of two superconducting regions separated by a thin oxide layer. Even if we are not interested in the full BCS theory [4], it is important to recall that the operating principle is based on quantum tunneling through the potential barrier given by the Cooper pairs, each of them is formed by an effective phonon-induced attraction of spin-opposite electrons, therefore they behave as bosonic particles [4]. It was proven that a realistic Hamiltonian of

a Josephson junction can be written as [4]

$$\hat{\mathcal{H}}_{jun} = \frac{\hat{Q}^2}{2C_q} - E_j \cos\Big[2\pi \frac{\hat{\Phi}}{\Phi_0}\Big] , \tag{1.14}$$

where C_q is the junction capacitance, E_J energy tunnel coupling and $\Phi_0 = \dfrac{h}{2e}$ the flux quantum.

Various kinds of flux qubit have been designed [4, 24]. The simplest form consists of a superconductor loop in which a Josephson junction is present. That loop is taken into account with an inductance. The circuit diagram of the flux qubit is reported in Fig. 1.2.

The total Hamiltonian will be written as

$$\hat{\mathcal{H}}_q = \frac{\hat{Q}_q^2}{2C_q} + \frac{\hat{\Phi}_q^2}{2L_q} - E_j \cos\Big[\frac{2\,\pi}{\Phi_0}(\hat{\Phi}_q - \Phi_{ext})\Big] , \tag{1.15}$$

tuning the magnetic field flux Φ_{ext} corresponds to modifying the potential

$$U(\hat{\Phi}_q) = \frac{\hat{\Phi}_q^2}{2L_q} - E_j \cos\Big[\frac{2\,\pi}{\Phi_0}(\hat{\Phi}_q - \Phi_{ext})\Big] ; \tag{1.16}$$

this applied flux is significantly affected by noise, whereas charge fluctuations do not affect the qubit. Note that the total flux, which is known as fluxoid Φ' [24], contained in the superconductor ring can be expressed as

$$\Phi' = n\Phi_0 , \tag{1.17}$$

with n an integer number.

It is possible to find two distinct working points from Eq. (1.17):

1. Choosing $\Phi_{ext} = n\Phi_0$, the energy spectrum would be characterized by a single level well-separated from the others. This configuration corresponds to the zero flowing current and is suitable for state preparation [4].

2. On the other hand, the worthwhile characteristics of our treatment would be observed by setting $\Phi_{ext} \approx (n + \frac{1}{2}\Phi_0)$. As can be appreciated

in Fig. 1.3 [24], the potential can be considered as a double well, in particular symmetric for $f = 0.5$ and asymmetric moving away from that particular point. Now, it is evident that the first two levels are separated from the others, which will not affect the dynamic of the system. Thus, the Hilbert space can be safely truncated to the first two states (*qubit approximation*); provided that $E_j \approx 10E_c$, where $E_c = \dfrac{(2e)^2}{2C_q}$ is the charging energy for a Cooper pair [24].

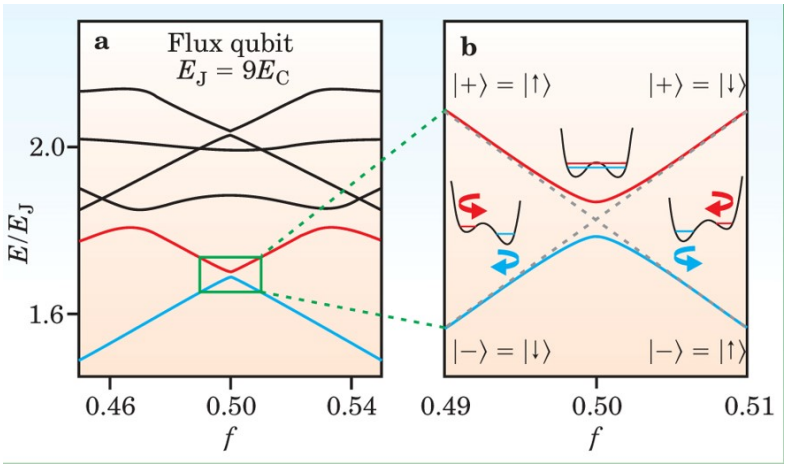

Figure 1.3: **Flux qubit energy levels as function of $f = \Phi_{ext}/\Phi_0$. (a)** Six energy levels are plotted. **(b)** Enlarged vision of the first two energy levels about f=0.50. The dashed line exhibits a crossing point that would occur if $E_J = 0$, the degeneration is lifted by the tunnel coupling (avoided level crossing). The image is taken from Ref. [24]. Although it concerns a three-junction flux qubit, their number affects only the sensitivity to flux noise because of the proper loop inductance required [24].

From now on, f is close to 0.5 and the two-level approximation will be considered valid. The double-well potential system in quantum mechanics is addressed by Ref. [25]. The Hamiltonian of the flux qubit could be expressed through the states $|L\rangle$ and $|R\rangle$ [16, 17] (see Fig. 1.4) that represent the two persistent currents flowing in opposite directions throughout the superconductive loop to produce an additional flux component, so the total flux

satisfies Eq. (1.17). As [25] states, it is possible to write:

$$\hat{\mathcal{H}}_q = \frac{\hbar}{2}\left(-\Delta\,\hat{\rho}_x + \epsilon\hat{\rho}_z\right), \tag{1.18}$$

where Δ is the tunnel splitting between the two different states, and $\epsilon = 2I_p(\Phi_{ext} - \frac{1}{2}\Phi_0)$ is the energy bias that is proportional to the flux applied and it can be easily visualized as the asymmetry of the double potential well when $\Delta = 0$. Furthermore, I_p is the maximum persistent current that the circuit can sustain until the non-dissipative dynamics breaks.

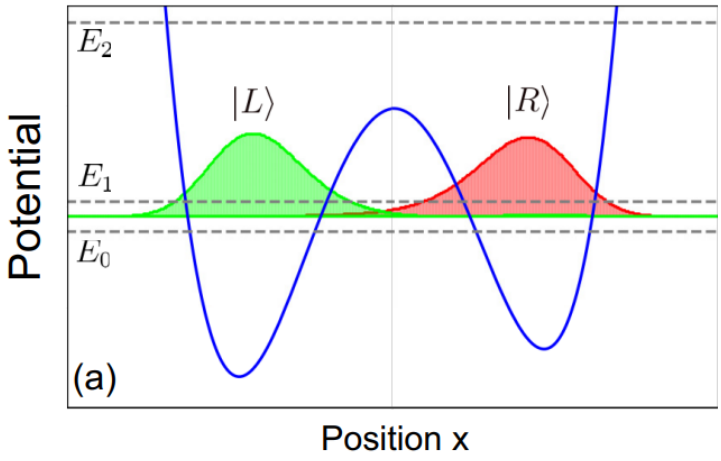

Figure 1.4: **The panel shows the double-well potential** in which the first two levels are well separated from the others. Furthermore, in this case, the position x should have been replaced by the flux. The green curve is the square modulus of the wave function located in the left well, whereas the red curve refers to the one in the right well. These two states are equivalent to persistent currents that flow oppositely throughout the superconductive loop. Image from Ref. [25].

The Pauli matrices of Eq. (1.18) are expressed in the $\{|L\rangle, |R\rangle\}$ basis. $\hat{\mathcal{H}}_q$ is straightforwardly diagonalized by the following procedure. We begin with writing the two by two $\mathcal{H}_q$ matrix:

$$\mathcal{H}_q = \frac{\hbar}{2}\begin{pmatrix} \epsilon & -\Delta \\ -\Delta & -\epsilon \end{pmatrix}. \tag{1.19}$$

To compute the eigenvectors and eigenvalues, specific angles are usually defined as [26]

$$\tan\theta = \frac{\Delta}{\epsilon} \quad \text{with} \quad 0 \leq \theta < \pi\,, \tag{1.20}$$

and $\varphi = \pi$ in this case. Substituting in Eq. (1.19):

$$\mathcal{H}_q = \frac{\hbar}{2}\,\epsilon \begin{pmatrix} 1 & \tan\theta\, e^{-i\pi} \\ \tan\theta\, e^{i\pi} & -1 \end{pmatrix}. \tag{1.21}$$

Finally, the two-qubit eigenvalues are trivially derived from the characteristic polynomial $E^2 - 1 - \tan^2\theta = 0$:

$$E_\pm = \pm\frac{\hbar}{2}\sqrt{\Delta^2 + \epsilon^2}\,. \tag{1.22}$$

It is evident that the energy spacing between the two levels is related to the so-called Larmor frequency $\sqrt{\Delta^2 + \epsilon^2}$ [16].
Regarding the eigenvectors, we have:

$$\begin{pmatrix} 1 & \tan\theta\, e^{-i\pi} \\ \tan\theta\, e^{+i\pi} & -1 \end{pmatrix} \begin{pmatrix} a \\ b \end{pmatrix} = \pm\frac{1}{\cos\theta} \begin{pmatrix} a \\ b \end{pmatrix}, \tag{1.23}$$

which gives the following condition:

$$\left(1 \mp \frac{1}{\cos\theta}\right) a + (\tan\theta\, e^{-i\pi})\, b = 0\,. \tag{1.24}$$

Trigonometry half-angle formulae permit, for the excited and ground state respectively, to rearrange Eq. (1.24) into:

$$\sin\frac{\theta}{2} a + \cos\frac{\theta}{2}\, b = 0\,, \tag{1.25a}$$

$$\cos\frac{\theta}{2} a - \sin\frac{\theta}{2}\, b = 0\,. \tag{1.25b}$$

Now, we can determine the eigenvectors of H_q imposing the normalization

condition:

$$|e\rangle = -\cos\frac{\theta}{2}\,|L\rangle + \sin\frac{\theta}{2}\,|R\rangle\ , \tag{1.26}$$

$$|g\rangle = \cos\frac{\theta}{2}\,|R\rangle + \sin\frac{\theta}{2}\,|L\rangle\ . \tag{1.27}$$

Hence, $|g\rangle$ and $|e\rangle$ are the qubit Hamiltonian eigenstates.

1.3 Galvanic coupling

Since all theoretical tools have been introduced, we can now describe the whole system. As occurs in cavity QED models, the single LC resonator mode can interact with the flux qubit via different kinds of coupling; in this case, we will focus on the galvanic fashion, which means both the qubit and the LC share an inductance L_c [16, 17, 27] (Fig. 1.5).

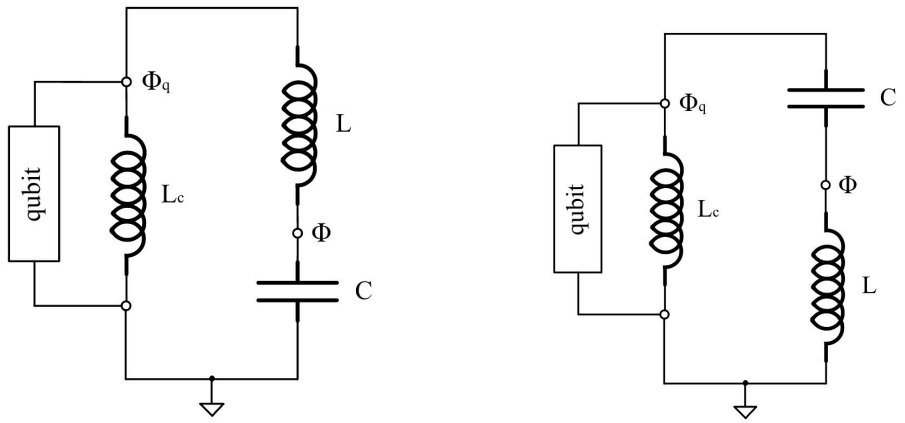

Figure 1.5: **Flux qubit inductively coupled to an LC resonator.** The choice of the ground determines the Hamiltonian structure. In panel **a**, the circuit is described by a Hamiltonian in the *flux gauge*. In the panel **b**, it is shown a circuit configuration described by the Hamiltonian in the *charge gauge*. Both pictures depict the qubit as a *black box*.

As was pointed out in Sec. 1.1, the quantization of a superconducting electric circuit is strictly dependent on the significant nodes and mainly on

the ground. This reasoning leads to two different scenarios: the so-called *flux gauge* and *charge gauge* [15, 17, 28]. In principle, it is common knowledge that physical measurable estimates must be gauge invariant. Choosing the charge coupling or the circuit configuration in Fig. 1.5b (charge gauge), the total Hamiltonian can be derived by applying a kind of minimal coupling replacement of type $\hat{Q}_q \rightarrow \hat{Q}_q + \hat{Q}$ in the flux Hamiltonian (the subscript q indicates the operators associated with the qubit) [15, 29]. Then, the truncation of Hilbert space would introduce some non-local potential, thus causing some problems in the gauge invariant theory; this issue was resolved by [29].

The charge gauge is much more problematic. By eventually performing the proper unitary transformation, it turns out a Hamiltonian that contains hyperbolic functions of operators, as shown by [29]. Thus, we prefer to adopt the flux gauge due to numerical reasons.
That said, the nodes used for quantization of the circuit are shown in Fig. 1.5a and, following the procedure that was illustrated in Sec. 1.1, we would obtain [15]:

$$\mathcal{L}_{tot} = \mathcal{L}_q + \mathcal{L}_{LC} + \frac{1}{L}\Phi\Phi_q \,. \tag{1.28}$$

Regarding Eq. (1.28), $\mathcal{L}_{LC}$ is identical to Eq. (1.3),

$$\mathcal{L}_q = C\,\frac{\dot{\Phi}_q^2}{2} - \frac{\Phi_q^2}{2L_q} + E_j \cos\left[\frac{2\,\pi}{\Phi_0}(\Phi_q - \Phi_{ext})\right] .$$

The inductance L_q is approximately equal to $\dfrac{L_c\,L_r}{L_c + L_r}$ [15], where the contribution of the superconductive loop has been neglected.
The conjugate momenta are:

$$\frac{\partial \mathcal{L}_{tot}}{\partial \dot{\Phi}} = C\dot{\Phi} = Q\,; \tag{1.29}$$

$$\frac{\partial \mathcal{L}_{tot}}{\partial \dot{\Phi}_q} = C_q\dot{\Phi}_q = Q_q\,. \tag{1.30}$$

Carrying out the Legendre transformation and promoting the canonical variables to operators, the total Hamiltonian of the circuit in the flux gauge will

be determined:

$$\hat{\mathcal{H}}_{tot} = \hat{\mathcal{H}}_q + \hat{\mathcal{H}}_{LC} - \frac{\hat{\Phi}\,\hat{\Phi}_q}{L}\,, \tag{1.31}$$

where $\hat{\mathcal{H}}_{LC}$ coincides with Eq. (1.5), $\hat{\mathcal{H}}_q$ to Eq. (1.15).

In Sec. 1.2 the two-level approximation concerning the flux qubit was proven to be robust, so we can project the entire Hamiltonian in the two-dimensional Hilbert space. In detail, choosing the persistent currents basis ($\{|L\rangle,|R\rangle\}$), Eq. (1.31) becomes [16, 27]

$$\hat{\mathcal{H}}_{tot} = \frac{\hbar}{2}\left(-\Delta\,\hat{\rho}_x + \epsilon\hat{\rho}_z\right) + \hbar\omega_r\left(\hat{a}^\dagger\,\hat{a} + \frac{1}{2}\right) + \hbar\omega_r\,\eta(\hat{a}^\dagger + \hat{a})\hat{\rho}_z\,, \tag{1.32}$$

in which the normalized coupling corresponds to $\eta = \dfrac{L_c I_p I_{zpf}}{\hbar\omega_r}$, where the zero point current fluctuations, related to the LC resonator, is equal to $\dfrac{\Phi_{zpf}}{L}$. Hence, maximizing I_p and selecting the proper inductance of the resonator, high coupling values are reachable, which was experimentally achieved by [16]. Finally, the entire dynamics can be decomposed by qubit, LC resonator, and magnetic interaction ($\mathcal{H}_{int} = -\vec{\mu}\cdot\vec{B}$) [27] terms.

It is more convenient to express Eq. (1.32) using the diagonal basis ($\{|g\rangle,|e\rangle\}$). To begin with, the relations that give $|g\rangle$ and $|e\rangle$ as linear combinations of $|L\rangle$ and $|R\rangle$ are trivially derived by relying on Eq. (1.26) and Eq. (1.27):

$$|L\rangle = \sin\frac{\theta}{2}\,|g\rangle - \cos\frac{\theta}{2}\,|e\rangle\ , \tag{1.33}$$

$$|R\rangle = \sin\frac{\theta}{2}\,|e\rangle + \cos\frac{\theta}{2}\,|g\rangle\ . \tag{1.34}$$

$\hat{\rho}_z$ will be rotated in the following manner:

$$\begin{aligned}\hat{\rho}_z^{(e,g)} = &\left(\sin\frac{\theta}{2}\,|g\rangle - \cos\frac{\theta}{2}\,|e\rangle\right)\left(\sin\frac{\theta}{2}\,\langle g| - \cos\frac{\theta}{2}\,\langle e|\right) + \\ &- \left(\sin\frac{\theta}{2}\,|e\rangle + \cos\frac{\theta}{2}\,|g\rangle\right)\left(\sin\frac{\theta}{2}\,\langle e| + \cos\frac{\theta}{2}\,\langle g|\right)\end{aligned} \tag{1.35}$$

that is

$$\hat{\rho}_z^{(e,g)} = \cos\theta\,\hat{\sigma}_z - \sin\theta\,\hat{\sigma}_x\,; \tag{1.36}$$

where $\hat{\sigma}_z$ and $\hat{\sigma}_x$ are the Pauli matrices expressed in the diagonal basis. Therefore:

$$\hat{\mathcal{H}}_{tot} = \frac{\hbar\omega_0}{2}\hat{\sigma}_z + \hbar\omega_r \hat{a}^\dagger \hat{a} + \hbar\omega_r \, \eta(\hat{a}^\dagger + \hat{a})\hat{\tilde{\sigma}}_x \, ; \tag{1.37}$$

ω_0 is the Larmor frequency, $\hat{\tilde{\sigma}}_x = (\cos\theta \, \hat{\sigma}_z - \sin\theta \, \hat{\sigma}_x)$, where $\cos\theta = \dfrac{\epsilon}{\omega_0}$ and $\sin\theta = \dfrac{\Delta}{\omega_0}$. The full Hamiltonian now resembles a typical quantum Rabi model, to be more precise, if $\epsilon = 0$.

Equation (1.37) represents the first key point in our treatment. We would like to stress that it is far from our aim to provide a detailed analysis regarding the picture of the circuit. If the reader is interested in a more in-depth description, we advise to examine [17].

Chapter 2

Quantum open system

Chapter 1 covers only a part of the story; we theoretically dealt with the LC resonator, a flux qubit, and their interaction resembling, due to the proper assumptions, the general Rabi model in quantum optics. However, the objective is to define the incoherent dynamics; that is, we must account for the interaction of the system (or subsystems) with an environment (reservoir) (see Fig. 2.1). For this purpose, the Schrödinger equation is not adequate, and then a master equation must be introduced. Depending on the degree of light-matter coupling, insidious elements could emerge.

The standard master equation, which is the most employed in quantum optical systems, can be expressed as (from this point $\hbar = 1$ for the sake of simplicity) [18–20]

$$\frac{d}{dt}\hat{\rho} = -i\left[\hat{H}_S, \hat{\rho}\right] + \mathcal{L}_{bare}\,\hat{\rho}\,, \tag{2.1}$$

where $\hat{H}_S$ is the system Hamiltonian, in fact the first term in Eq. (2.1) is responsible for the Hamiltonian dynamic, $\hat{\rho}$ is the density matrix operator of the system, and $\mathcal{L}_{bare}$ is the Liouvillian superoperator that acts on $\hat{\rho}$ as follows [18–20, 30]:

$$\mathcal{L}_{bare}\,\hat{\rho} = \sum_i \left[\gamma_i(1 + n(\omega_i, T_i)\right]\mathcal{D}[\hat{s}_i]\hat{\rho} + \gamma_i\, n(\omega_i, T_i)\,\mathcal{D}[\hat{s}_i^\dagger]\hat{\rho}\,. \tag{2.2}$$

The index i in the summation of Eq. (2.2) is associated with a specific subsystem that interacts weakly with its respective independent reservoir, this process is characterized by a leakage rate γ_i. Furthermore, each reservoir is assumed to be in thermal equilibrium at a certain temperature T_i, and, as a

consequence, $n(\omega_i, T_i)$ is present in Eq. (2.2), which corresponds to the thermal photon population. The notation $\mathcal{D}[\hat{A}]$, where $\hat{A}$ is any system operators, indicates a dissipator, specifically [18, 19, 30]:

$$\mathcal{D}[\hat{A}]\hat{\rho} = \frac{1}{2}\left[2\hat{A}\hat{\rho}\hat{A} - \hat{\rho}\hat{A}^{\dagger}\hat{A} - \hat{A}^{\dagger}\hat{A}\hat{\rho}\right]. \tag{2.3}$$

For instance, $\hat{s}_i$ could be $\hat{a}$ and $\hat{\sigma}_-$, which is defined as $|g\rangle\langle e|$ on the diagonal basis, for the resonator and the qubit, respectively, while $\hat{s}_i^{\dagger}$ are $\hat{a}^{\dagger}$ and $\hat{\sigma}_+$. The standard master equation (Eq. (2.1)) is most reliable in circuit (cavity) QED applications, as long as the strength of the light-matter coupling ranges from weak to strong. As reported in panel **(a)** of Fig. 2.1, the derivation of dissipators in Eq. (2.3) does not consider the coupling between the light and matter subsystems [18–20].

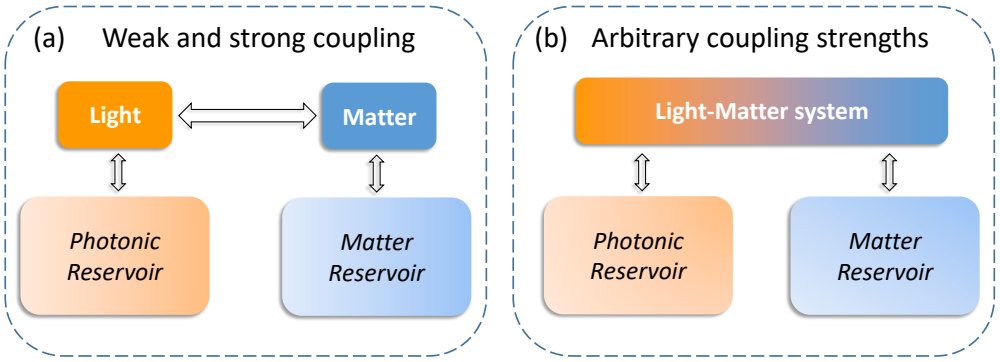

Figure 2.1: **(a) Master-equation approach valid in the weak and strong coupling regimes**: the standard master equation, which does not account for light-matter coupling to derive the dissipators, is valid in these regimes. **(b) The master-equation approach considering the light-matter coupling**. As the coupling strength between the two subsystems increases, it becomes necessary to treat dissipation effects, including the coupling between the subsystems. This can be done by developing the system operators that describe the coupling to the reservoirs in the eigenbasis of the coupled light-matter system. Scheme taken by [18].

On the other hand, applying the standard master equation when the ultra-strong (USC) and deep-strong (DSC) coupling are achieved, **non-physical** phenomena arise. [20] highlights how, even in the ground state (i.e.,

at $T = 0$) and in the ultrastrong coupling regime, the system would relax and it exhibits photon emission in the cavity, which is clearly not reasonable. In addition, computing emission spectra could be rather tricky. The panel **(b)** of Fig. 2.1 suggests that, in order to resolve this issue, the light-matter interaction must be included in the definition of dissipators.

2.1 Dressed and generalized master equation

2.1.1 Generalized master equation

In this section, we report the procedure for determining the generalized dressed master equation. Also, it will be shown, provided specific approximations and conditions, that the generalized dressed master equation coincides with the one proposed by [20]. To this end, we adopt the same method that is presented by [18–20] and, as has been done concerning the standard master equation, the analysis is purely general; then we are going into detail of our system.

It is always possible to decompose the full Hamiltonian as the sum of all terms, i.e., the system ($\hat{H}_S$), for instance, the quantum Rabi Hamiltonian, the reservoir ($\hat{H}_B$) and its weak interaction with the system ($\hat{H}_{SB}$):

$$\hat{H} = \hat{H}_S \otimes \hat{I}_B + \hat{H}_B \otimes \hat{I}_S + \hat{H}_{SB}\,, \tag{2.4}$$

$\hat{I}_B$ and $\hat{I}_S$ are the bath and system identity operator, respectively. As we considered earlier, the i-th reservoir (or bath) Hamiltonian can be written as a multi-mode harmonic oscillator. Each of them is labeled by an index l, and has a frequency ν_l with their respective creation ($\hat{b}$) and annihilation ($\hat{b}^\dagger$) operators. Hence:

$$\hat{H}_B^{(i)} = \sum_l \nu_l\, \hat{b}_l^\dagger\, \hat{b}_l\,. \tag{2.5}$$

Interaction Hamiltonian can be depicted in the following fashion:

$$\hat{H}_{SB} = \sum_{i,l}\ \alpha_{i,l}\,(\hat{b}_{i,l}^\dagger + \hat{b}_{i,l})(\hat{s}_i^\dagger + \hat{s}_i)\,; \tag{2.6}$$

where $\alpha_{i,l}$ is the coupling strength for the i-th subsystem to l-th mode, $\hat{s}_i$ (and $\hat{s}_i^\dagger$) comply with the definitions of Eq. (2.2) and Eq. (2.3).
Regardless of the regime of coupling between the subsystems, it is necessary to start with the motion equation of the total density matrix operator, namely, the Liouville equation [26]:

$$\frac{d}{dt}\hat{\tilde{\rho}} = -i\left[\hat{\tilde{H}}_{SB}, \hat{\tilde{\rho}}\right] . \tag{2.7}$$

The tilde over the operators stands for the interaction picture representation [19, 31], that is

$$\hat{\tilde{A}}(t) = e^{i(\hat{H}_S + \hat{H}_B)t}\, \hat{A}\, e^{-i(\hat{H}_S + \hat{H}_B)t} ; \tag{2.8}$$

where $\hat{A}$ is a general bath or system operator. A more convenient form of Eq. (2.7) can be expressed by

$$\hat{\tilde{\rho}}(t) - \hat{\tilde{\rho}}(0) = -i\int_0^t ds \left[\hat{\tilde{H}}_{SB}(s), \hat{\tilde{\rho}}(s)\right] , \tag{2.9}$$

and substituting it in Eq. (2.7), we obtain:

$$\frac{d}{dt}\hat{\tilde{\rho}}(t) = -i\left[\hat{\tilde{H}}_{SB}, \hat{\tilde{\rho}}(0)\right] - \int_0^t ds \left[\hat{\tilde{H}}_{SB}(t), \left[\hat{\tilde{H}}_{SB}(s), \hat{\tilde{\rho}}(s)\right]\right] . \tag{2.10}$$

Expectation values of the system's physical observables are commonly sought:

$$\langle \hat{O} \rangle = tr_S\big(\hat{O}\hat{\tilde{\rho}}_S\big) , \tag{2.11}$$

the subscript S in the trace indicates that is partially done over the system's Hilbert space. Furthermore, it has been defined the reduced density matrix [26] $\hat{\tilde{\rho}}_S$ as

$$\hat{\tilde{\rho}}_S = tr_B\big(\hat{\tilde{\rho}}\big) , \tag{2.12}$$

in this case the partial trace is performed over the degrees of freedom of the reservoir.
At this point, in order to focus on the dynamics of the system, the trace over the degrees of freedom of the reservoir is applied to both sides of Eq. (2.10),

so the Liouville equation becomes:

$$\frac{d}{dt}\hat{\tilde{\rho}}_S(t) = -i\,tr_B\big[\hat{\tilde{H}}_{SB}, \hat{\tilde{\rho}}(0)\big] - \int_0^t ds\, tr_B\Big[\hat{\tilde{H}}_{SB}(t), \big[\hat{\tilde{H}}_{SB}(s), \hat{\tilde{\rho}}(s)\big]\Big]\,. \quad (2.13)$$

However, we still have the total density matrix in the commutator of Eq. (2.13). Thus, *Born approximation* is conventionally employed [18,19], it is based on the weak coupling consideration between reservoir and system, therefore it is reasonable to decompose the total density matrix:

$$\hat{\tilde{\rho}}(t) = \hat{\tilde{\rho}}_S(t) \otimes \hat{\rho}_B\,. \quad (2.14)$$

Despite this assumption, excitations from the system to the reservoir still occur. Second, as according to [30], it is appropriate to evaluate $tr_B\big[\hat{\tilde{H}}_{SB}, \hat{\tilde{\rho}}(0)\big]$ as zero, since, at the initial time ($t = 0$), the reservoir could be evaluated in thermal equilibrium with its density matrix diagonal on the energy basis representation. Finally, another key point turns out to further simplify the dynamics, that is, *the Markov approximation* [18–20,30]. In practice, due to the realistic short decay time of the reservoir [30], the terms $\hat{\tilde{H}}_{SB}(t)\,\hat{\tilde{H}}_{SB}(s)$, and vice versa, are relevant solely for t roughly equal to s, hence it is not a surprise to assume $\hat{\tilde{\rho}}_S(s) = \hat{\tilde{\rho}}_S(t)$.
In summary, Eq. (2.13) turns to

$$\frac{d}{dt}\hat{\tilde{\rho}}_S(t) = -\int_0^t ds\, tr_B\Big[\hat{\tilde{H}}_{SB}(t), \big[\hat{\tilde{H}}_{SB}(s), \hat{\rho}_S(t) \otimes \hat{\tilde{\rho}}_B\big]\Big]\,, \quad (2.15)$$

which is known as the Redfield equation [19,30].
However, it is not a Markovian master equation yet [19], since it depends on the initial state of the system. To overcome this question, substitution $s \to t - s$ has to be performed, which is justified only if the characteristic time of an appreciable variation of the state of the system is significantly greater than the decay time of the correlation functions of the reservoir [19,30]. Finally, the upper limit of the integral (Eq. (2.15)) is imposed to infinity. Thus, the

Redfield equation becomes the Markov-Born master equation [19, 30]:

$$\frac{d}{dt}\hat{\tilde{\rho}}_S(t) = -\int_0^{+\infty} ds\, tr_B\left[\hat{\tilde{H}}_{SB}(t), \left[\hat{\tilde{H}}_{SB}(t-s), \hat{\tilde{\rho}}_S(t)\otimes\hat{\rho}_B\right]\right]. \tag{2.16}$$

Until now, standard approximations have been adopted; the true turning point is the projection of $\hat{\tilde{H}}_{SB}$ onto the *dressed basis* [18, 19], which is the representation that makes $\hat{H}_S$ diagonal. That equals writing the interaction picture system operators as

$$\begin{aligned}\hat{\tilde{S}}_i(t) &= \sum_{\epsilon'-\epsilon=\omega} e^{i(\hat{H}_S+\hat{H}_B)t}\,\hat{\Pi}(\epsilon)(\hat{s}_i+\hat{s}_i^\dagger)\,\hat{\Pi}(\epsilon')\,e^{i(\hat{H}_S+\hat{H}_B)t} = \\ &= \sum_{\epsilon'-\epsilon=\omega}\hat{\Pi}(\epsilon)(\hat{s}_i+\hat{s}_i^\dagger)\,\hat{\Pi}(\epsilon')\,e^{-i\omega t} = \sum_{\epsilon'-\epsilon=\omega}\hat{S}_i(\omega)\,e^{-i\omega t},\end{aligned} \tag{2.17}$$

where $\hat{\Pi}(\epsilon) = |\epsilon\rangle\langle\epsilon|$ is the projector operator on the respective $\hat{H}_S$ eigenstate having ϵ as eigenvalue. On this representation, $\hat{\tilde{S}}_i(t)$ is expressed as the sum of transition operators between different eigenstates with frequency spacing ω. A further distinction can be made on the basis of the sign of ω [18]:

$$\hat{S}_i^{(+)}(\omega) = \hat{S}_i(+\omega) \quad \text{for} \quad \omega > 0\,; \tag{2.18}$$

$$\hat{S}_i^{(-)}(\omega) = \hat{S}_i(-\omega) \quad \text{for} \quad \omega > 0\,; \tag{2.19}$$

$$\hat{S}_i^{(0)}(\omega) = \hat{S}_i(\ \ \omega) \quad \text{for} \quad \omega = 0\,. \tag{2.20}$$

Exchanging the reservoir operators with them in interaction picture [18],

$$\hat{\tilde{B}}_i(t) = \sum_l \alpha_{i,l}\,\hat{b}_{i,l}\,e^{-i\nu_l t}, \tag{2.21}$$

where $\hat{\tilde{B}}_i^\dagger$ is easily obtained from Eq. (2.21), $\hat{\tilde{H}}_{SB}(t)$ can be written as

$$\hat{\tilde{H}}_{SB}(t) = \sum_i \hat{\tilde{S}}_i(t)\left(\hat{\tilde{B}}_i(t) + \hat{\tilde{B}}_i^\dagger(t)\right). \tag{2.22}$$

The elements needed to derive the Markov-Born master equation are now available. For the sake of simplicity, we show the explicit computations in

Appendix A. Finally, the generalized master equation, stressing that the Lamb shift has been neglected, is written as

$$\dot{\hat{\rho}}_S = -i\left[\hat{H}_S, \hat{\rho}_S\right] + \mathcal{L}_g\,\hat{\rho}_S\,, \tag{2.23}$$

with

$$\begin{aligned}\mathcal{L}_g\,\hat{\rho}_S = \frac{1}{2}\sum_i\sum_{\omega,\omega'}\Big\{&\Gamma_i(-\omega')N(-\omega',T_i)[\hat{S}_i(\omega')\hat{\rho}_S(t)\hat{S}_i(\omega) - \hat{S}_i(\omega)\hat{S}_i(\omega')\hat{\rho}_S(t)]+\\
&+\Gamma_i(\omega)N(\omega,T_i)[\hat{S}_i(\omega')\hat{\rho}_S(t)\hat{S}_i(\omega) - \hat{\rho}_S(t)\hat{S}_i(\omega)\hat{S}_i(\omega')]+\\
&+\Gamma_i(\omega)[N(\omega,T_i)+1]\,[\hat{S}_i(\omega)\hat{\rho}_S(t)\hat{S}_i(\omega') - \hat{S}_i(\omega')\hat{S}_i(\omega)\hat{\rho}_S(t)]+\\
&+\Gamma_i(-\omega')[N(-\omega',T_i)+1][\hat{S}_i(\omega)\hat{\rho}_S(t)\hat{S}_i(\omega') - \hat{\rho}_S(t)\hat{S}_i(\omega')\hat{S}_i(\omega)]\Big\}.\end{aligned} \tag{2.24}$$

Additional considerations can be made. Provided the system energy levels are sufficiently separated, i.e. $\omega \gg \Gamma_i(\omega)$, a product of operators involving $\hat{S}_i^{(\pm)}(\omega)\,\hat{S}_i^{(\pm)}(\omega')$ and $S^{(0)}S_i^{(\pm)}(\omega)$ give rise to a fast oscillating term that can be discarded. This procedure takes the name of post-trace rotating-wave approximation (RWA) [18], thus, Eq. (A.20) is reduced to

$$\begin{aligned}\mathcal{L}_g\,\hat{\rho}_S = \frac{1}{2}\sum_i\sum_{(\omega,\omega')>0}\Big\{&\Gamma_i(\omega')N(\omega',T_i)[\hat{S}_i^{(-)}(\omega')\hat{\rho}_S(t)\hat{S}_i^{(+)}(\omega) - \hat{S}_i^{(+)}(\omega)\hat{S}_i^{(-)}(\omega')\\
&\times\hat{\rho}_S(t)] + \Gamma_i(\omega)N(\omega,T_i)[\hat{S}_i^{(-)}(\omega')\hat{\rho}_S(t)\hat{S}_i^{(+)}(\omega) - \hat{\rho}_S(t)\hat{S}_i^{(+)}(\omega)\hat{S}_i^{(-)}(\omega')]\\
&+\Gamma_i(\omega)[N(\omega,T_i)+1][\hat{S}_i^{(+)}(\omega)\hat{\rho}_S(t)\hat{S}_i^{(-)}(\omega') - \hat{S}_i^{(-)}(\omega')\hat{S}_i^{(+)}(\omega)\hat{\rho}_S(t)]+\\
&+\Gamma_i(\omega')[N(\omega',T_i)+1][\hat{S}_i^{(+)}(\omega)\hat{\rho}_S(t)\hat{S}_i^{(-)}(\omega') - \hat{\rho}_S(t)\hat{S}_i^{(-)}(\omega')\hat{S}_i^{(+)}(\omega)]+\\
&+\Omega_i^{+}(T_i)[\hat{S}_i^{(0)}\hat{\rho}_S(t)\hat{S}_i^{(0)} - \hat{S}_i^{(0)}\hat{S}_i^{(0)}\hat{\rho}_S(t)] + \Omega_i'^{+}(T_i)[\hat{S}_i^{(0)}\hat{\rho}_S(t)\hat{S}_i^{(0)}+\\
&-\hat{\rho}_S(t)\hat{S}_i^{(0)}\,\hat{S}_i^{(0)}] + \Omega_i^{-}(T_i)[\hat{S}_i^{(0)}\hat{\rho}_S(t)\hat{S}_i^{(0)} - \hat{\rho}_S(t)\hat{S}_i^{(0)}\hat{S}_i^{(0)}]+\\
&+\Omega_i'^{-}(T_i)[\hat{S}_i^{(0)}\hat{\rho}_S(t)\hat{S}_i^{(0)} - \hat{S}_i^{(0)}\hat{S}_i^{(0)}\hat{\rho}_S(t)]\,.\end{aligned} \tag{2.25}$$

In conclusion, this description, which was conducted by [18], is completely generalized. It can be used in several cases, for example, when the in-

teraction with the environment of cavity (and circuit) QED systems exhibits anharmonic, anharmonic-harmonic mixed spectra in whatever **coupling strength** [18]. Moreover, it takes into account degenerate transitions that determine pure dephasing terms.
As highlighted by [20], Eq. (2.25) does not respect a Lindblad form; therefore, the positivity and probability conservation of the density matrix are not certain. The suggested solution of these stability problems consists of applying to the Lindbladian a filter function.

2.1.2 Dressed master equation

For the sake of completeness, the author of [20] proposed a dressed master equation that shed light on ultrastrong coupling regime questions regarding cavity (circuit) QED, which were discussed at the beginning of chapter 2.
The general approach is similar to that of Sec. 2.1.1, but several differences establish specific application conditions. In detail, an initial RWA approximation is performed when the interaction Hamiltonian between the system and the bath is introduced. Furthermore, [20] studied a system with parity symmetry, whereas the generalized master equation derivation ([18]) does not comply with that. As a consequence, transition element such as C_{jj} are zero, where

$$C_{jj} = \left\langle j \left| \hat{c} + \hat{c}^{\dagger} \right| j \right\rangle \; ; \tag{2.26}$$

with $\hat{c}$ ($\hat{c}^{\dagger}$) photon creation (annihilation) operator. Thus, in other words, degenerate transitions are discarded.
Then, in order to derive the dressed master equation, they applied the classical Born-Markov approximation and took a bath described by a continuum of frequencies. In addition, a secular approximation has been employed. If $|\omega' - \omega|^{-1}$ (for $\omega \neq \omega'$) is greater than the characteristic relaxation time of the reservoir τ_R, the oscillating factors for $\omega' \neq \omega$ can be ignored, as stated by [19, 20]. In the end, the dressed master equation suits **only** to an open quantum system that displays anharmonic spectrum with parity symmetry and pure dephasing terms are excluded.

2.2 Coupling with a transmission line

In this section, a flux qubit coupled to an LC oscillator that is connected to a transmission line through a mutual inductance is first analyzed. Then, the second case concerns the same scheme, but the transmission line is capacitively coupled to the oscillator-qubit circuit.

2.2.1 Quantization of a transmission line

To begin with, it is convenient to consider just an open transmission line and the aim is to derive the characteristic Hamiltonian.

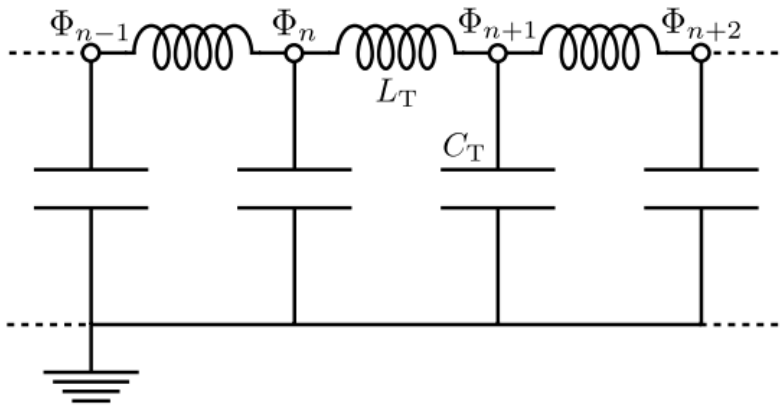

Figure 2.2: **Telegraph model of a lossless transmission line [15].**

The telegraph model ([32]) establishes that a transmission line, such as a coplanar waveguide resonator, can be described as a sequence of elementary two port components, namely inductors, capacitors, and resistors. However, as can be inferred by Fig. 2.2, resistors are absent due to the almost lossless nature typical of circuit QED applications. Once LC Hamiltonian has been computed, determining the classical one of a transmission line is straightforward:

$$H_{tl} = \sum_{i=0}^{N-1} \left[\frac{Q_n^2}{2\,C_T} - \frac{(\Phi_{n+1} + \Phi_n)^2}{2\,L_T} \right]. \tag{2.27}$$

C_T and L_T are the capacitance and inductance relative to each "site", where homogeneity in the TL (transmission line) is assumed. Moreover, it is com-

mon to define the same electric quantities per unit length [32]:

$$c_T = \frac{C_T}{\delta_x}\,, \tag{2.28}$$

$$l_T = \frac{L_T}{\delta_x}\,. \tag{2.29}$$

That said, passing to continuum limit is equivalent to taking the limit of δ_x to zero, so Eq. (2.27) turns to

$$H_{tl} = \int_0^d dx \left[\frac{\rho_Q^2(x)}{2\,c_T} + \left(\frac{\partial\Phi(x)}{\partial x}\right)^2 \frac{1}{2\,l_T}\right], \tag{2.30}$$

where $\rho_Q(x) = Q_n/\delta_x$ is the charge density field and $\Phi(x) = \Phi_n$ the continuum flux field ([15,32]). The charge density field is related to the generalized variable, the flux, through its time derivative $\big(\rho_Q(x,t) = c_T\partial_t\Phi(x,t)\big)$. Furthermore, note that, conversely to the case of an LC resonator, a transmission line is a distributed element.

By applying Hamilton's equations, propagation through the TL is expressed via wave equation:

$$\frac{\partial^2\Phi(x,t)}{\partial t^2} = v_0^2\,\frac{\partial^2\Phi(x,t)}{\partial x^2}\,, \tag{2.31}$$

where $v_0 = 1/\sqrt{c_T\,l_T}$ is the speed of light in the TL.

Imposing the proper boundary condition, based on the type of resonator, permits to decompose the classical Hamiltonian in a series of harmonic oscillators with different characteristic frequencies ω_m. Then, considering the canonical quantization, it turns out

$$\hat{H}_{tl} = \sum_{m=0}^{\infty} \omega_m\,\hat{b}_m^\dagger\,\hat{b}_m\,; \tag{2.32}$$

as shown by [32], $\omega_m = (m+1)\omega_0$ (where $\omega_0 \approx v_0/2d$) concerning a $\lambda/2$ TL.

2.2.2 Inductive coupling

The circuit diagram of a transmission line coupled by mutual inductance to the system depicted in Sec. 1.3 is reported in Fig. 2.3. Now, the total classical Hamiltonian is composed by the TL term, qubit-LC one and the interaction between them via mutual inductance M ([15]):

$$\begin{aligned} H_{tot} = H_q + \frac{Q^2}{2\,C} + \frac{1}{2\,\tilde{L}}\,\Phi^2 + \frac{1}{2\,L}(\Phi - \Phi_q)^2 + \\ + \frac{1}{2\,C_T}\sum_{j=1} Q_j^2 + \frac{1}{2\tilde{L}_T}(\Phi_{n+1} - \Phi_n)^2 + \frac{1}{2\,L_T}\sum_{j\neq n}(\Phi_{j+1} - \Phi_j)^2 + \\ + \frac{\Phi - \Phi_q}{2\,\tilde{M}}\,(\Phi_{n+1} - \Phi_n)\,. \end{aligned} \tag{2.33}$$

where H_q is the qubit Hamiltonian (for example, Eq. (1.15)). It is immediately recognizable how the first line describes the qubit, the LC oscillator, and their galvanic interaction in the flux gauge. The second line contains the

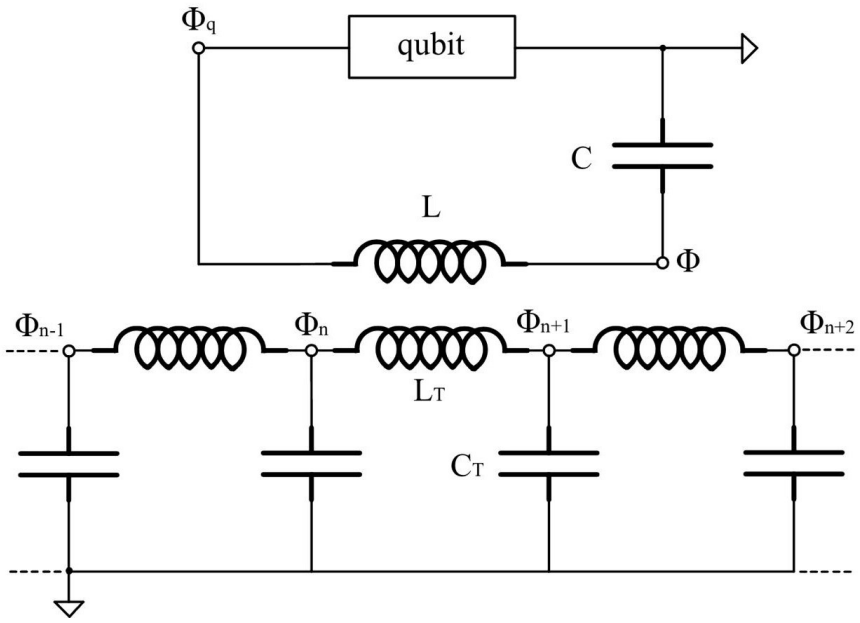

Figure 2.3: **Circuit diagram of a transmission line coupled via a mutual inductance M to a flux qubit-LC circuit**. The location of the ground fixes the gauge choice, that is **flux gauge**.

factors regarding the transmission line. Finally, the last element depicts the coupling of the LC resonator with the TL by means of $\tilde{M} = L\,L_T - M^2/M$ (effective inductance). Furthermore, rescaled inductors $\tilde{L}$ and $\tilde{L}_T$ are introduced in Eq. (2.33). The first is equal to $L\,L_T - M^2/L_T$, the latter to $L\,L_T - M^2/L$. If the aim is to carry out QND (quantum non-destructive) measurements ([2, 33]), a common design choice is taking $M \ll L$, as indicated by [15] . Under that condition, $\tilde{L}$ and $\tilde{L}_T$ can be evaluated with their original values. Then, the continuum limit regarding the TL and canonical quantization are performed. To avoid confusion, the flux along the TL is labeled as $\hat{\phi}(x)$. When the system is reduced to the first two states (two-level or qubit approximation), the qubit flux $\hat{\Phi}_q$ projected on the qubit basis can be roughly written as $2\eta\tilde{\sigma}_x$ ([15]). Reminding that the flux of resonator is expressed by Eq. (1.11), Eq. (2.33) becomes:

$$\hat{H}_{tot} = \hat{H}_{fg} + \hat{H}_{tl} + \hat{V}_{ind}\,, \tag{2.34}$$

where $\hat{H}_{fg}$ is the Hamiltonian of Eq. (1.37), $\hat{H}_{tl}$ is the quantized version of Eq. (2.27), and

$$\hat{V}_{ind} = \alpha\Phi_{zpf}\,(\hat{a} + \hat{a}^\dagger - 2\eta\,\tilde{\sigma}_x)\int dx\,\frac{\partial\hat{\phi}(x)}{\partial x}\,, \tag{2.35}$$

with $\alpha = M/L\,L_T$. The flux $\hat{\phi}(x)$ operator can be expressed as [15, 32]

$$\hat{\phi}(x) = \int_0^{+\infty} d\omega\,\frac{\Lambda}{\sqrt{\omega}}\big(\hat{b}_\omega\,e^{ik_\omega x} + \hat{b}^\dagger_\omega\,e^{-ik_\omega x}\big)\,, \tag{2.36}$$

where $\Lambda = \sqrt{Z_0/4\pi}$, with Z_0 being the TL impedance. Furthermore, $k_\omega = \omega/v_0$ is the wave number. At this point, assuming the LC resonator is placed at $x = 0$, the interaction can be written as:

$$\hat{V}_{ind} = i\,\frac{1}{\Phi_{zpf}}\,\hat{\Phi}_L\int_0^{+\infty} d\omega\,\alpha\Phi_{zpf}\,\frac{\Lambda}{v_0}\,\sqrt{\omega}\,[\hat{b}_\omega - \hat{b}^\dagger_\omega]\,, \tag{2.37}$$

with $\hat{\Phi}_L = \hat{a} + \hat{a}^\dagger - 2\eta\,\hat{\tilde{\sigma}}_x$.

2.2.3 Capacitive coupling

TL capacitively coupled to the LC-qubit circuit may represent an alternative scheme (see Fig. 2.4).

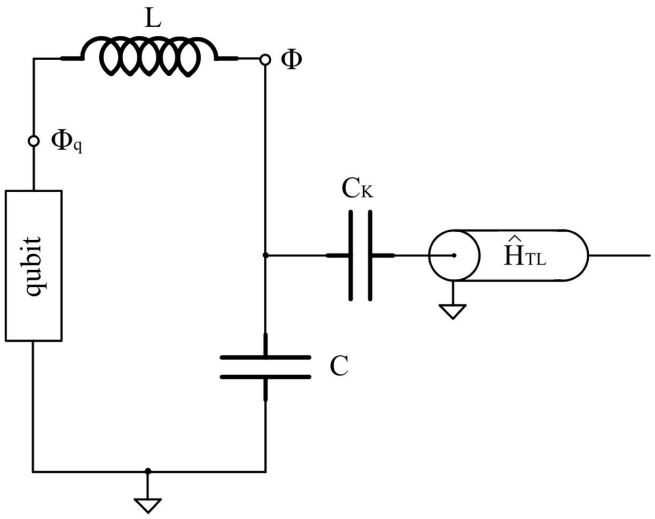

Figure 2.4: **A semi-infinite transmission line coupled through a capacitor C_K to the LC-qubit circuit.**

In order to avoid redundancy, the focus is on the significant difference from Sec. 2.2.2, that lies in the interaction Hamiltonian. In this case, as a result of the coupling, the operator involved is the product of the canonical momentum charge of the transmission line and the canonical momentum charge of the LC. Thus, a suitable interaction Hamiltonian is derived by [27]:

$$\hat{V}_{cap} = \int_{-\infty}^{+\infty} dx\, \delta(x) \frac{1}{C_T} \frac{C_k}{C}\, \hat{Q}\, \hat{\rho}_Q(x)\,, \tag{2.38}$$

where delta function is because of the LC resonator located at $x = 0$, C_k is the capacitor that connects the TL to the LC oscillator (Fig. 2.4). To be more precise, renormalization of C_T, C, and C_k should be applied; however, the procedure can be neglected.

Substituting all terms, it results

$$\hat{V}_{cap} = \int_0^{+\infty} d\omega \, \frac{C_k}{\sqrt{C}} \sqrt{\frac{\omega \, \omega_r}{2\pi \, v_0 \, C_T}} \, i(\hat{b}_\omega - \hat{b}_\omega^\dagger) \, i(-\hat{a} + \hat{a}^\dagger) \, . \tag{2.39}$$

In the end, it is recognizable that the capacitive or inductive coupling corresponds to the treatment that has been conducted regarding quantum open systems. In fact, for instance, performing the following transformation

$$\hat{b}_\omega \to i \, \hat{b}_\omega \, , \tag{2.40}$$

Eq. (2.37) and Eq. (2.39) can be connected to $\hat{H}_{SB}$ of Sec. 2.1.1 (interaction Hamiltonian system-reservoir) without modifying Eq. (2.32).

Chapter 3

Numerical results

The starting block is to numerically diagonalize the Hamiltonian of the flux qubit-LC circuit (Eq. (1.37)):

$$\hat{\mathcal{H}}_S = \frac{\omega_0}{2}\hat{\sigma}_z + \omega_r\big(\hat{a}^\dagger\,\hat{a}\big) + \omega_r\,\eta(\hat{a}^\dagger + \hat{a})\hat{\tilde{\sigma}}_x\,, \tag{3.1}$$

recalling $\hat{\tilde{\sigma}}_x = (\cos\theta\,\hat{\sigma}_z - \sin\theta\,\hat{\sigma}_x)$, where $\cos\theta = \dfrac{\epsilon}{\omega_0}$ and $\sin\theta = \dfrac{\Delta}{\omega_0}$ (Chapter.1).

Before reporting the diagram of its eigenvalues, note that $\hat{\mathcal{H}}_S$ has two free parameters: the normalized coupling η and the energy bias (which is related to the flux offset) ϵ. Experiments that involve this configuration usually fix η, while ϵ is tuned [16,17,34]. It is fundamental to remember that ϵ controls the qubit frequency ω_0 ($\sqrt{\Delta^2+\epsilon^2}$) and is related to the qubit-LC interaction ($\cos\theta = \dfrac{\epsilon}{\omega_0}$). Hence, we fix the normalized coupling and the energy eigenvalues are computed as a function of ϵ, the idea is to verify how *ultrastrong coupling* modifies the *incoherent dynamics*.

3.1 Strong coupling

Firstly, we choose $\eta = 0.05$ and $\Delta/\omega_r = 3$ was imposed. Fig. 3.1 displays $\omega_{\tilde{1},\tilde{0}}$ (blue curve) and $\omega_{\tilde{4},\tilde{0}}$ (orange curve). They represent the energy transitions of the ground state to the first and fourth states, respectively. Moreover, we label the eigenstates of Eq. (3.1) $|\tilde{J}\rangle$ (J is an integer), the energy increases as J does. We plotted only the differences between eigenvalues that will be

significant later on.

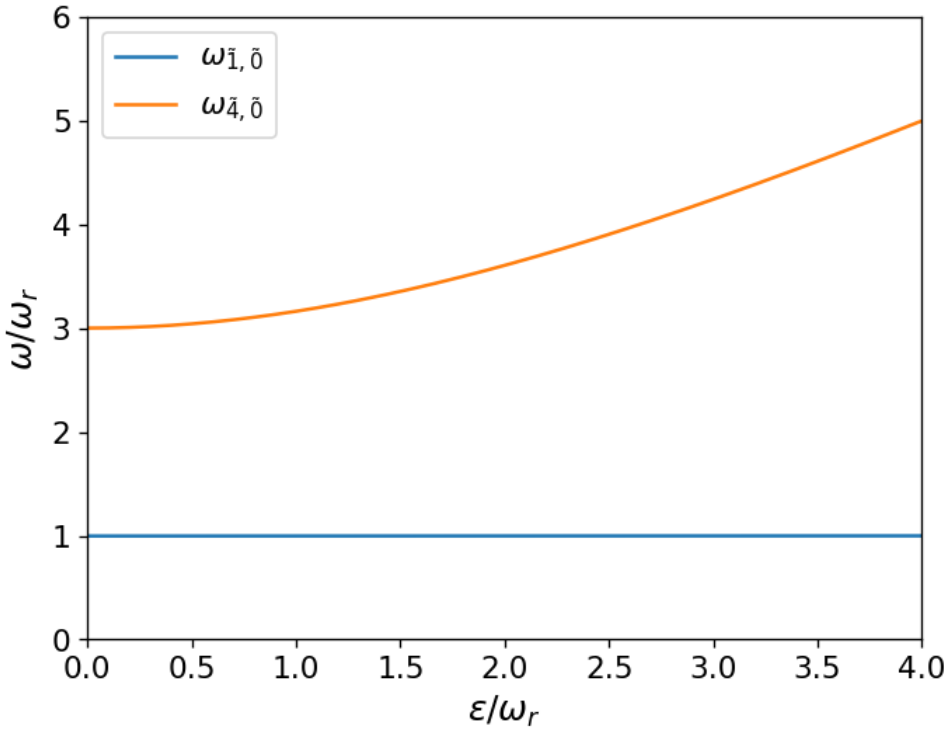

Figure 3.1: **Energy levels as function of** ϵ/ω_r. There are visualized only the first (blue curve) and the fourth energy levels (orange curve), the ground state energy has been subtracted to both.

The objective is now to compute **emission spectra**, which can give an idea concerning the incoherent dynamics of the system, namely, the frequencies of photons emitted. Power spectrum function is written as Fourier transform of the correlation function regarding a system operator [35, 36]:

$$S(\omega) = Re \int_0^{+\infty} d\tau \left\langle \hat{X}^{(-)}(t+\tau)\hat{X}^{(+)}(t) \right\rangle_{ss} e^{-i\omega\tau}, \tag{3.2}$$

where $\hat{X}^{(\pm)}$ follow the definition of Eq. (2.18) and Eq. (2.19). In fact, taking the positive and negative frequencies component of a system operator $\hat{X}$, which is projected on the *dressed basis* $|\tilde{J}\rangle$, guarantees avoiding misleading results in the ultrastrong coupling regime.

By selecting the proper operator $\hat{X}$, it is possible to calculate the emission spectrum $S(\omega)$ either of the LC resonator (or cavity) or of the qubit. The *ss* subscript of Eq. (3.2) indicates that the correlation function has to be evaluated for the *steady state*, which is found numerically and is related to the particular form of the Liouvillian superoperator (Eq. (2.25)); hence the generalized master equation must be explicated. Since we want to simulate the coupling with a transmission line, an ohmic reservoir suits the task. As introduced by [18], the relations determining the ohmic bath are:

$$\Gamma_i(\omega) = \gamma_i \, \frac{\omega}{f_i} \, ; \tag{3.3}$$

$$\Omega_i^{'(\pm)}(T_i) = \Omega_i^{(\pm)}(T_i) = \frac{\gamma_i}{4\, f_i} \, T_i \, . \tag{3.4}$$

γ_i are the damping rates of the subsystems and their frequencies are equal to f_i. Expanding the summation of Eq. (2.25), Eq. (2.23) becomes

$$\dot{\hat{\rho}}_S = -i \left[\hat{H}_S, \hat{\rho}_S \right] + \mathcal{L}_g \, \hat{\rho}_S \, , \tag{3.5}$$

with $\mathcal{L}_g \, \hat{\rho}_S$:

$$\begin{aligned}
\mathcal{L}_g \, \hat{\rho}_S = \frac{1}{2} \sum_{(\omega,\omega')>0} \Bigg\{ & \frac{\gamma_q \omega'}{\omega_0} N(\omega', T_q) [\hat{P}^{(-)}(\omega') \hat{\rho}_S(t) \hat{P}^{(+)}(\omega) - \hat{P}^{(+)}(\omega) \hat{P}^{(-)}(\omega') \\
& \times \hat{\rho}_S(t)] + \frac{\gamma_q \omega}{\omega_0} N(\omega, T_q) [\hat{P}^{(-)}(\omega') \hat{\rho}_S(t) \hat{P}^{(+)}(\omega) - \hat{\rho}_S(t) \hat{P}^{(+)}(\omega) \hat{P}^{(-)}(\omega')] \\
& + \frac{\gamma_q \omega}{\omega_0} [N(\omega, T_q) + 1] [\hat{P}^{(+)}(\omega) \hat{\rho}_S(t) \hat{P}^{(-)}(\omega') - \hat{P}^{(-)}(\omega') \hat{P}^{(+)}(\omega) \hat{\rho}_S(t)] + \\
& + \frac{\gamma_q \omega'}{\omega_0} [N(\omega', T_q) + 1] [\hat{P}^{(+)}(\omega) \hat{\rho}_S(t) \hat{P}^{(-)}(\omega') - \hat{\rho}_S(t) \hat{P}^{(-)}(\omega') \hat{P}^{(+)}(\omega)] + \\
& + \frac{\gamma_q}{\omega_0} \, T_q [\hat{P}^{(0)} \hat{\rho}_S(t) \hat{P}^{(0)} - \frac{1}{2} \hat{P}^{(0)} \hat{P}^{(0)} \hat{\rho}_S(t) - \frac{1}{2} \, \hat{\rho}_S(t) \hat{P}^{(0)} \, \hat{P}^{(0)}] + \\
& + \frac{\gamma_r \omega}{\omega_r} [\hat{A}^{(+)}(\omega) \hat{\rho}_S(t) \hat{A}^{(-)}(\omega') - \hat{A}^{(-)}(\omega') \hat{A}^{(+)}(\omega) \hat{\rho}_S(t)] + \\
& + \frac{\gamma_r \omega'}{\omega_r} [\hat{A}^{(+)}(\omega) \hat{\rho}_S(t) \hat{A}^{(-)}(\omega') - \hat{\rho}_S(t) \hat{A}^{(-)}(\omega') \hat{A}^{(+)}(\omega)] \Bigg\} \, .
\end{aligned} \tag{3.6}$$

In Eq. (3.6), γ_r and γ_q are the damping rates of the resonator and the qubit,

respectively. The effective temperature of the resonator is zero, as a consequence, the factors that are proportional to the mean number of thermal photons ($N(\omega, T_r) = 0$) disappeared, whereas we consider a reservoir interacting with the qubit at an effective temperature $T_q \neq 0$. Concerning the numerical values, $\gamma_r/\omega_r = 10^-3$, $\gamma_q/\omega_r = 10^-3$ and $T_q/\omega_r = 0.07$. Being $\eta \gg \{\gamma_r/\omega_r, \gamma_q/\omega_r\}$, but still $\eta < 0.1$, it is realistic to assess the regime of interaction as *strong coupling*; as shown by [3].

What remains is defining the operators that play a role in Eq. (3.6) and in the power spectrum function (Eq. (3.2)), distinctions have to be made between the capacitive coupling with a TL or the inductive one. The operators that constitute the Liouvillian superoperator can be easily inferred by the interaction of the system Hamiltonian with the TL (see Eq. (2.39) and Eq. (2.37)). Regarding the emission spectra, it is usual to measure the tension $\hat{V}_L$ on the inductor L for the inductive coupling with the TL [15], whereas $\hat{V}_C$ for the capacitive coupling. $\hat{V}_C$ corresponds to Eq. (1.13). Obtaining $\hat{V}_L$ equals to computing the time derivative of $\hat{\Phi}_L$ (Eq. (2.37)):

$$\hat{V}_L = i\left[\hat{H}_S, \hat{\Phi}_L\right] = -2\omega_0\eta \,\sin\theta\,\hat{\sigma}_y + i\omega_r\,(\hat{a}^\dagger - \hat{a})\,. \tag{3.7}$$

Also, we consider the qubit interacting with an ohmic bath with $\tilde{\sigma}_x$ acting as dissipation operator ($\hat{P}$). In summary:

	Inductive	**Capacitive**
η	0.05	0.05
γ_r/ω_r	10^{-3}	10^{-3}
γ_q/ω_r	10^{-3}	10^{-3}
T_q/ω_r	0.07	0.07
T_r/ω_r	0	0
Δ/ω_r	3	3
$\hat{X}$	$-2\omega_0\eta\,\sin\theta\,\hat{\sigma}_y + i\omega_r\,(\hat{a}^\dagger - \hat{a})$	$i(\hat{a}^\dagger - \hat{a})$
$\hat{P}$	$\hat{\tilde{\sigma}}_x$	$\hat{\tilde{\sigma}}_x$
$\hat{A}$	$\hat{a} + \hat{a}^\dagger - 2\eta\,\hat{\tilde{\sigma}}_x$	$i(\hat{a}^\dagger - \hat{a})$

Table 3.1: Parameters and operators used for the capacitively and inductively coupled LC-qubit circuit to a TL.

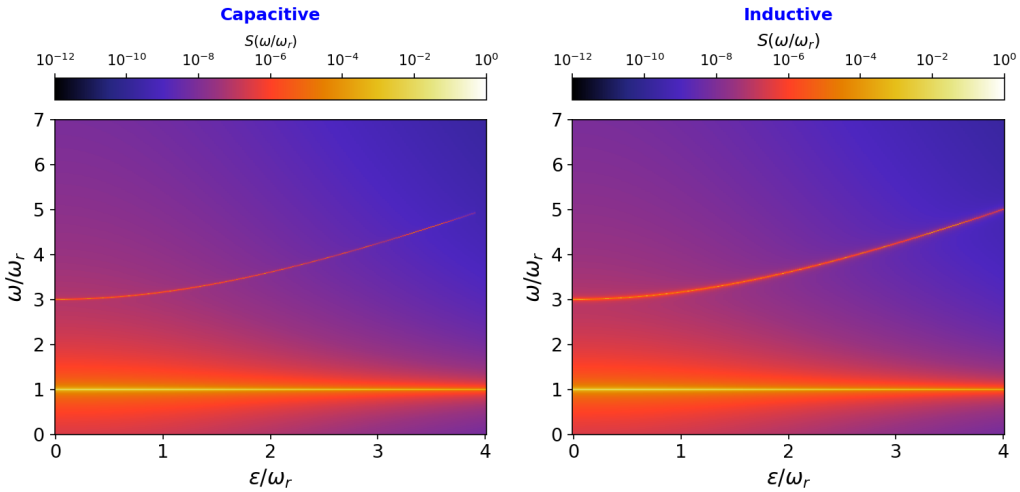

Figure 3.2: **2-D emission spectra** obtained by numerically computing $S(\omega)$ (Eq. (3.2)) at the steady state. The capacitive and the inductive emission spectra are computed by using the operators and parameters of Table 3.1. Both figures depict the power spectrum function, which is represented in a logarithmic scale, as functions of ω and ϵ that changes the qubit frequency. Furthermore, the spectra were normalized with respect to the maximum value of the capacitive one. The transition lines are those of Fig. 3.1.

In the end, the emission spectra of Fig. 3.2 highlight the transitions that are reported in Fig. 3.1, $\omega_{\tilde{1},\tilde{0}}$ and $\omega_{\tilde{4},\tilde{0}}$. Furthermore, since $\Delta/\omega_r = 3$ and $\omega_0 = \sqrt{\Delta^2 + \epsilon^2}$, when ϵ/ω_r increases, the detuning, $\delta = |\omega_r - \omega_0|$, will be larger; even for $\epsilon = 0$ the LC circuit and the qubit are off resonance. That condition is often useful to perform QND measurements, it also defines the *dispersive regime*.

As expected, in the strong coupling regime, no differences arise from the different ways of coupling the system to the external world. To be certain of that, we proceed to plot the one-dimensional spectra attained by fixing a specific value of ϵ. Selecting $\epsilon = 0$ (see Fig. 3.3a), capacitive and inductive emission spectra are identical. Fig. 3.3b follows the same pattern. However, the second peak, which is associated with $\omega_{\tilde{4},\tilde{0}}$, moves towards higher frequencies. That is a trivial consequence of increasing ϵ.

In conclusion, when the strong coupling regime holds, no variations will be revealed, as predicted. Jaynes-Cummings model [3] is still valid and, in fact,

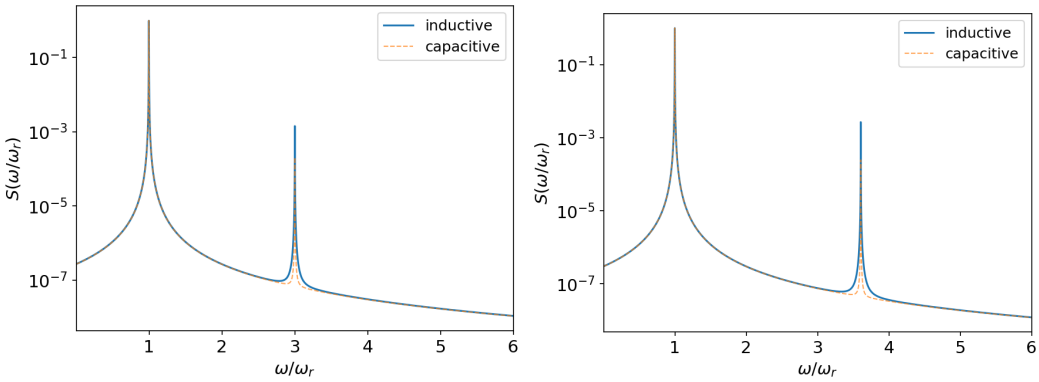

(a) (b)

Figure 3.3: **1-dimensional emission spectra** for $\eta = 0.05$ and $T_q/\omega_r = 0.07$.
Panel **(a)** is made by fixing $\epsilon = 0$, whereas panel **(b)** for $\epsilon = 2$. The spectra were normalized with respect to the maximum value of the capacitive one, moreover, $S(\omega)$ is plotted in a logarithmic scale.

it is immediate to recognize the spectral lines, which are visualized in Fig. 3.2. At the frequency of ω_r, $\omega_{\tilde{1},\tilde{0}}$ can be associated with the transition from the one photon state ($|\tilde{1}\rangle \simeq |1, g\rangle$) to the ground state ($|\tilde{0}\rangle \simeq |0, g\rangle$), similarly, $\omega_{\tilde{4},\tilde{0}}$ from the excited state of the qubit ($|\tilde{4}\rangle \simeq |0, e\rangle$) to the ground state ($|\tilde{0}\rangle \simeq |0, g\rangle$).

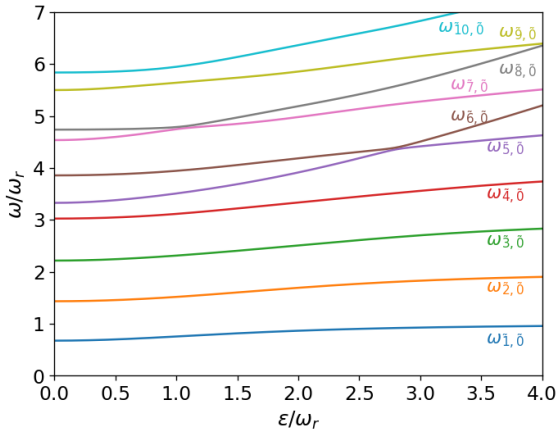

Figure 3.4: **Energy level transitions for** $\eta = 0.7$. The figure shows the energy transitions, from the first excited state up to the eighth, down to the ground state.

3.2 Ultrastrong coupling

It is known that ultrastrong coupling is achieved when $\eta \geq 0.1$ [3]. Therefore, $\eta = 0.7$ should be sufficient to observe any kind of variation between the two approaches. The procedure is identical. Firstly, the transitions of the energy levels down to the ground state are displayed in Fig. 3.4. As done before, the list of parameters and operators concerning this case are indicated in Table 3.2

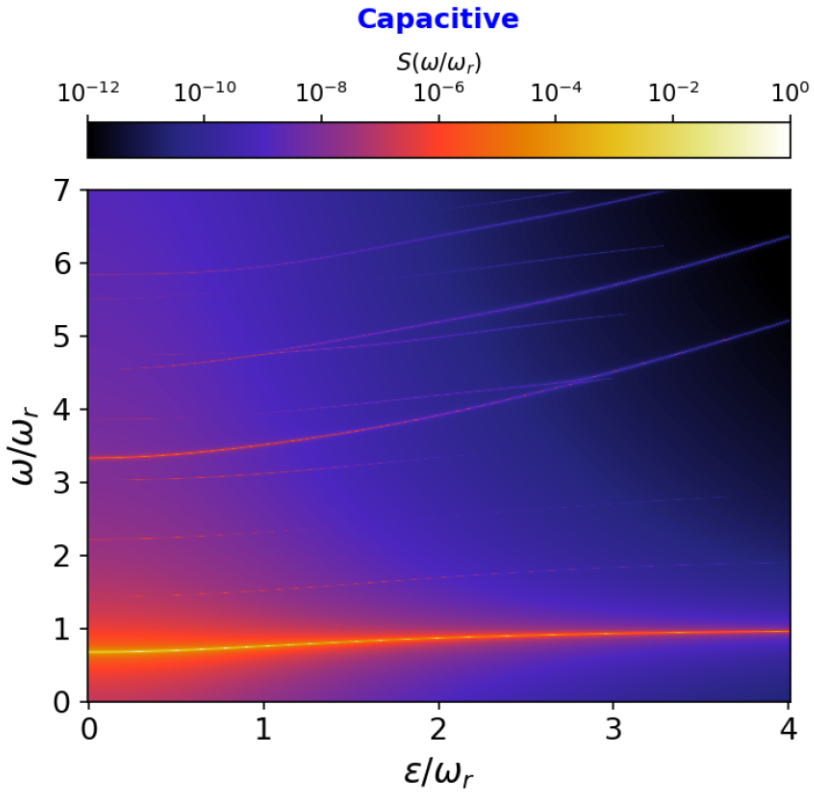

Figure 3.5: **Capacitive 2-dimensional emission spectrum for operators and parameters given by Table 3.2**. It is obtained by numerically computing $S(\omega)$ (Eq. (3.2)) at the steady state. The spectrum lines are those of Fig. 3.4.

	Inductive	**Capacitive**
η	0.7	0.7
γ_r/ω_r	10^{-3}	10^{-3}
γ_q/ω_r	10^{-3}	10^{-3}
T_q/ω_r	0.07	0.07
T_r/ω_r	0	0
Δ/ω_r	3	3
$\hat{X}$	$-2\omega_0\eta \sin\theta\, \hat{\sigma}_y + i\omega_r\,(\hat{a}^\dagger - \hat{a})$	$i(\hat{a}^\dagger - \hat{a})$
$\hat{P}$	$\hat{\tilde{\sigma}}_x$	$\hat{\tilde{\sigma}}_x$
$\hat{A}$	$\hat{a} + \hat{a}^\dagger - 2\eta\,\hat{\tilde{\sigma}}_x$	$i(\hat{a}^\dagger - \hat{a})$

Table 3.2: Parameters and operators used for the capacitively and inductively coupled LC-qubit circuit to a TL.

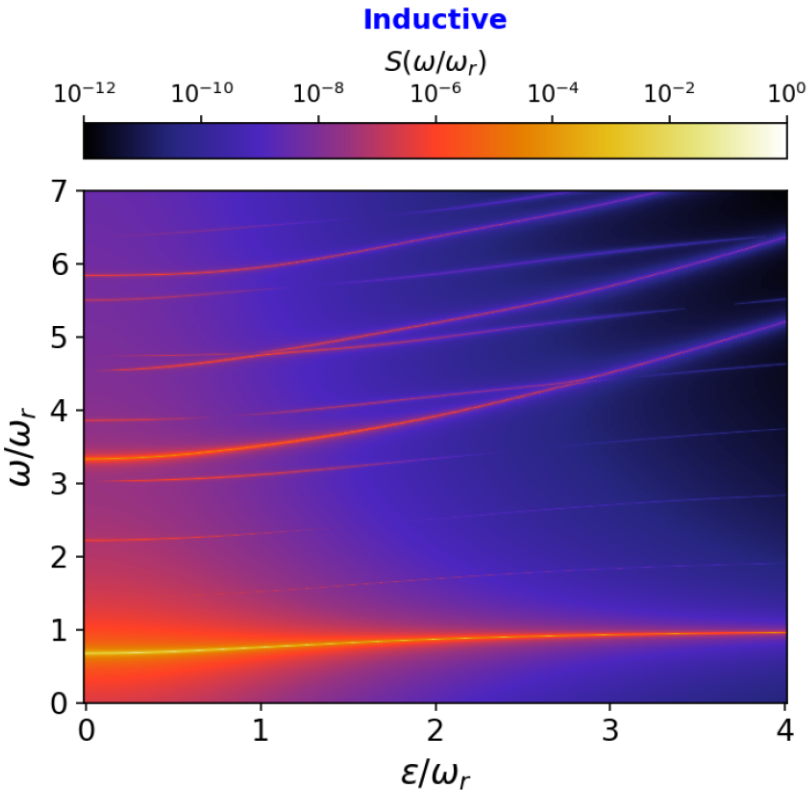

Figure 3.6: **Inductive 2-dimensional emission spectrum for operators and parameters given by Table 3.2**. It is obtained by numerically computing $S(\omega)$ (Eq. (3.2)) at the steady state. The spectrum lines are those of Fig. 3.4.

At first glance, emission spectra (see Fig. 3.6 and Fig. 3.5) feature variations in the two methods. Fixing ϵ, the attention is focused on the 1-dimensional spectra.

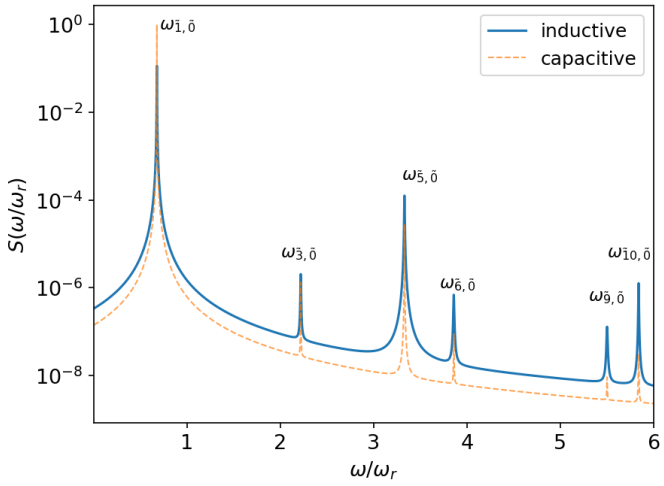

Figure 3.7: **1-dimensional emission spectra for $\eta = 0.7$, $T_q/\omega_r = 0.07$ and $\epsilon = 0$.** The spectra were normalized with respect to the maximum value of the capacitive one; furthermore, $S(\omega)$ is plotted on a logarithmic scale.

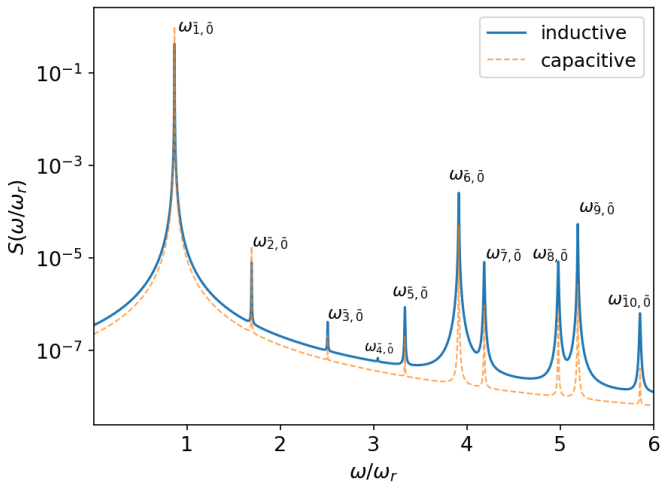

Figure 3.8: **1-dimensional emission spectra for $\eta = 0.7$, $T_q/\omega_r = 0.07$ and $\epsilon = 2$.** The spectra were normalized with respect to the maximum value of the capacitive one; furthermore, $S(\omega)$ is plotted on a logarithmic scale.

At last, Fig. 3.7 and Fig. 3.8 clarify the situation:

- In general, the "qubit-like" peaks are more prominent concerning the inductive coupling. To be more specific, for $\epsilon = 0$, $\omega_{\tilde{5},\tilde{0}}$, $\omega_{\tilde{6},\tilde{0}}$, $\omega_{\tilde{9},\tilde{0}}$, and $\omega_{\tilde{10},\tilde{0}}$ exhibit this feature. The same applies to $\omega_{\tilde{5},\tilde{0}}$, $\omega_{\tilde{6},\tilde{0}}$, $\omega_{\tilde{7},\tilde{0}}$, $\omega_{\tilde{8},\tilde{0}}$, $\omega_{\tilde{9},\tilde{0}}$ and $\omega_{\tilde{10},\tilde{0}}$, when $\epsilon = 2$. This characteristic could be ascribed to the presence of a background.

- However, the most curious result is related to the width of the peaks. Inductive coupling presents "qubit-like" peaks that have much larger widths compared to the corresponding capacitive, even showing an FWHM (full width half maximum) greater than the leakage rates that were imposed.

In Appendice B we present the code and other cases that take into account intermediate coupling strength in the ultrastrong coupling regime.

Conclusions

In this work, we studied the emission properties of a circuit QED system constituted by a flux qubit coupled with an LC resonator in the USC regime. In particular, we analyzed the emission of photons from the LC circuit under incoherent excitations of the artificial atom. We considered the circuit QED system out of thermal equilibrium, with the qubit coupled to a reservoir at an effective temperature T_q different from zero, and the electromagnetic resonator T_c such that $T_c << T_q$. Moreover, we investigated how the nature (capacitive or inductive) of the coupling of the LC oscillator with the output port influences the emission properties.

In summary, in Chapter1, we addressed the quantization of the superconducting circuit considered, which is a flux qubit inductively coupled to an LC resonator.

Then, to describe the incoherent dynamics, we employed a generalized master equation approach [18] suitable for quantum optical systems displaying light-matter interactions reaching the *ultrastrong coupling* regime.

We used the numerically calculated steady state of the density matrix to compute the emission spectra out from the electromagnetic resonator, considering both the inductive and capacitive coupling to the output port. When the light-matter interaction is sufficiently large (USC regime), we observed significant variations between the two configurations, as shown in Chp.3. The results, under the condition of strong detuning (*dispersive regime*) between the LC resonator and the qubit, show:

- A stronger amplitude of the "qubit-like" emission peaks for the inductive coupling with respect to the capacitive one.

- When η increases, the linewidths of the inductive "qubit-like" peaks are larger than those obtained for the capacitive coupling.

The results presented here are still preliminary and deserve further analysis. A very interesting feature is that these results highlight some peculiar properties of circuit QED systems not present in the corresponding cavity-QED systems, although the two settings can be formally described by identical Hamiltonians.

As a future development, it would be interesting to apply the same formalism considering a coherent drive instead of incoherent pumping. Moreover, we observe that the system here investigated can present innovative nonlinear optical effects that should be explored.

Acknowledgments— We acknowledge the Army Research Office (ARO) (Grant No. W911NF1910065).

Appendices

Appendix A

Derivation of Markov-Born generalized master equation

To begin with the derivation of the explicit Markov-Born generalized master equation [18], it is necessary to expand the commutator of Eq. (2.16), we would have

$$\begin{aligned}\frac{d}{dt}\hat{\tilde{\rho}}_S(t) = &-\int_0^{+\infty} ds\, tr_B\{\hat{\tilde{H}}_{SB}(t)\,\hat{\tilde{H}}_{SB}(t-s)\,\hat{\tilde{\rho}}_S(t)\otimes\hat{\rho}_B + \\ &- \hat{\tilde{H}}_{SB}(t-s)\,\hat{\tilde{\rho}}_S(t)\otimes\hat{\rho}_B\,\hat{\tilde{H}}_{SB}(t) + \\ &- \hat{\tilde{H}}_{SB}(t)\,\hat{\tilde{\rho}}_S(t)\otimes\hat{\rho}_B\,\hat{\tilde{H}}_{SB}(t-s) + \\ &+ \hat{\tilde{\rho}}_S(t)\otimes\hat{\rho}_B\,\hat{\tilde{H}}_{SB}(t-s)\;\hat{\tilde{\rho}}_S(t)\}\,.\end{aligned} \tag{A.1}$$

Each row of Eq. (A.1) can be expanded further by means of Eq. (2.22). For instance, we compute the first row:

$$\begin{aligned}= &-\int_0^{+\infty} ds \sum_{i,j} tr_B\Big\{\Big[\hat{\tilde{S}}_i(t)\,\hat{\tilde{B}}_i(t)\,\hat{\tilde{S}}_j(t-s)\,\hat{\tilde{B}}_j(t-s) + \\ &+ \hat{\tilde{S}}_i(t)\,\hat{\tilde{B}}_i(t)\,\hat{\tilde{S}}_j(t-s)\,\hat{\tilde{B}}_j^\dagger(t-s) + \hat{\tilde{S}}_i(t)\,\hat{\tilde{B}}_i^\dagger(t)\,\hat{\tilde{S}}_j(t-s)\,\hat{\tilde{B}}_j(t-s) + \\ &+ \hat{\tilde{S}}_i(t)\,\hat{\tilde{B}}_i^\dagger(t)\,\hat{\tilde{S}}_j(t-s)\,\hat{\tilde{B}}_j^\dagger(t-s)\Big]\hat{\tilde{\rho}}_S(t)\otimes\hat{\rho}_B\Big\}\,.\end{aligned} \tag{A.2}$$

The trace is performed on the reservoir Hilbert space, therefore working out the expectation values for every reservoir operators corresponds to

$$\left\langle \hat{\tilde{O}}_{bath} \right\rangle = tr_B\{\hat{\tilde{O}}_{bath}\,\hat{\rho}_B\}. \tag{A.3}$$

Furthermore, it can be easily shown

$$\left\langle \hat{\tilde{B}}_i \hat{\tilde{B}}_j^\dagger \right\rangle \neq 0 \quad \text{only if} \quad i = j\,; \tag{A.4}$$

$$\left\langle \hat{\tilde{B}}_i^\dagger \hat{\tilde{B}}_j \right\rangle \neq 0 \quad \text{only if} \quad i = j\,; \tag{A.5}$$

$$\left\langle \hat{\tilde{B}}_i^\dagger \hat{\tilde{B}}_j^\dagger \right\rangle = \left\langle \hat{\tilde{B}}_i \hat{\tilde{B}}_j \right\rangle = 0\,; \tag{A.6}$$

these relations are valid due to the mutual independence of the various reservoirs and the expectation values of the creation and annihilation operators, as we will observe. That said, Eq. (A.2) is reduced to

$$\begin{aligned} = -\int_0^{+\infty} ds \sum_i \Big\{ & \hat{\tilde{S}}_i(t)\, \hat{\tilde{S}}_i(t-s) \hat{\tilde{\rho}}_S(t) \left\langle \hat{\tilde{B}}_i(t) \hat{\tilde{B}}_i^\dagger(t-s) \right\rangle + \\ & + \hat{\tilde{S}}_i(t)\, \hat{\tilde{S}}_i(t-s) \hat{\tilde{\rho}}_S(t) \left\langle \hat{\tilde{B}}_i^\dagger(t) \hat{\tilde{B}}_i(t-s) \right\rangle \Big\}. \end{aligned} \tag{A.7}$$

The remaining terms of Eq. (A.1) can be effortlessly derived, reminding of the cyclic property of the density matrix. Thus:

$$\begin{aligned} \frac{d}{dt}\hat{\tilde{\rho}}_S(t) = -\int_0^{+\infty} ds \sum_i \Big\{ & \left(\hat{\tilde{S}}_i(t-s) \hat{\tilde{\rho}}_S(t)\, \hat{\tilde{S}}_i(t) - \hat{\tilde{S}}_i(t) \hat{\tilde{S}}_i(t-s) \hat{\tilde{\rho}}_S(t) \right) \times \\ & \times \left\langle \hat{\tilde{B}}_i^\dagger(t) \hat{\tilde{B}}_i(t-s) \right\rangle + \left(\hat{\tilde{S}}_i(t) \hat{\tilde{\rho}}_S(t)\, \hat{\tilde{S}}_i(t-s) - \hat{\tilde{\rho}}_S(t)\, \hat{\tilde{S}}_i(t-s) \hat{\tilde{S}}_i(t) \right) \times \\ & \times \left\langle \hat{\tilde{B}}_i^\dagger(t-s) \hat{\tilde{B}}_i(t) \right\rangle + \left(\hat{\tilde{S}}_i(t-s) \hat{\tilde{\rho}}_S(t)\, \hat{\tilde{S}}_i(t) - \hat{\tilde{S}}_i(t) \hat{\tilde{S}}_i(t-s) \hat{\tilde{\rho}}_S(t) \right) \times \\ & \times \left\langle \hat{\tilde{B}}_i(t) \hat{\tilde{B}}_i^\dagger(t-s) \right\rangle + \left(\hat{\tilde{S}}_i(t) \hat{\tilde{\rho}}_S(t)\, \hat{\tilde{S}}_i(t-s) - \hat{\tilde{\rho}}_S(t)\, \hat{\tilde{S}}_i(t-s) \hat{\tilde{S}}_i(t) \right) \times \\ & \times \left\langle \hat{\tilde{B}}_i(t-s) \hat{\tilde{B}}_i^\dagger(t) \right\rangle \Big\}. \end{aligned} \tag{A.8}$$

Defining the explicit form of the reservoir density matrix is required to determine the correlation functions of Eq. (A.8). Note that, as reported in

Sec. 2.1, the reservoir can be assumed to be at thermal equilibrium, hence

$$\hat{\rho}_B = \frac{e^{-\beta \hat{H}_b}}{tr_B \left[e^{-\beta \hat{H}_b} \right]} , \tag{A.9}$$

where $\beta = \dfrac{1}{k_B T}$. Recalling that reservoir Hamiltonian is given by Eq. (2.5), the density matrix can be written as

$$\hat{\rho}_B = \prod_l \left(1 - e^{-\beta \nu_l}\right) e^{-\beta \nu_l \hat{b}_l^\dagger \hat{b}_l} . \tag{A.10}$$

Eq. (A.10) and Eq. (2.21) allow us to compute the reservoir correlation functions. These calculations are quite convoluted, and we are not going to show them. Given that we are dealing with product of annihilation and creation operators, the only non-zero expectation values correspond to the following relations:

$$\left\langle \hat{b}_l \, \hat{b}_{l'}^\dagger \right\rangle = \delta_{l,l'} (1 + N(\nu_l, T)) , \tag{A.11}$$

$$\left\langle \hat{b}_l^\dagger \, \hat{b}_{l'} \right\rangle = \delta_{l,l'} N(\nu_l, T) , \tag{A.12}$$

$$N(\nu_l, T) = \frac{1}{e^{\frac{\nu_l}{T}} - 1} . \tag{A.13}$$

$N(\nu_l, T)$ represents the mean number of thermal photons. Moreover, the discrete frequency modes will become a continuous variable by extending the quantization volume to infinity. Eventually, it results

$$\left\langle \hat{\tilde{B}}_i^\dagger(t) \hat{\tilde{B}}_i(t-s) \right\rangle = \int_0^{+\infty} d\nu \, g_i(\nu) |\alpha_i(\nu)|^2 \, N(\nu, T_i) e^{i\nu s} , \tag{A.14}$$

$$\left\langle \hat{\tilde{B}}_i(t) \hat{\tilde{B}}_i^\dagger(t-s) \right\rangle = \int_0^{+\infty} d\nu \, g_i(\nu) |\alpha_i(\nu)|^2 \, [N(\nu, T_i) + 1] e^{-i\nu s} , \tag{A.15}$$

where $g_i(\nu)$ is the density of states of the $i-th$ reservoir. If the first term of Eq. (A.8) is expanded, it will be attained

$$= \int_0^{+\infty} \sum_i \sum_{\omega,\omega'} ds\, e^{-i(\omega+\omega')t} e^{i\omega' s} [\hat{S}_i(\omega')\hat{\tilde{\rho}}_S(t)\hat{S}_i(\omega) - \hat{S}_i(\omega)\hat{S}_i(\omega')\hat{\tilde{\rho}}_S(t)] \times \int_0^{\infty} d\nu\, g_i(\nu)\, |\alpha_i(\nu)|^2\, N(\nu, T_i)\, e^{i\nu s}\,. \tag{A.16}$$

The key is to resolve the double integral in Eq. (A.16) [19]:

$$\int_0^{+\infty} ds\, e^{-i(\nu-\omega)s} = \pi\delta(\nu-\omega) - i\mathcal{P}\frac{1}{\nu-\omega}\,, \tag{A.17}$$

$\mathcal{P}$ indicates the Cauchy principal value and it will be eventually the source of Lamb shift of the energy levels [19, 20]. In fact, a system Hamiltonian would require a renormalization. However, the Lamb shift is not included in our treatment because of the negligible shifts implied, as [20] states.
The same proceeding leads to the derivation of the other terms of Eq. (A.8). Furthermore, the representation of operators is switched from interaction to Schrödinger picture, thus simplifying factors such as $e^{-i(\omega+\omega')t}$. In the end, it turns out:

$$\dot{\hat{\rho}}_S = -i\left[\hat{H}_S, \hat{\rho}_S\right] + \mathcal{L}_g\, \hat{\rho}_S\,, \tag{A.18}$$

$\mathcal{L}_g$ is the Lindbladian superoperator defined as [18]

$$\begin{aligned}\mathcal{L}_g\, \hat{\rho}_S = \frac{1}{2}\sum_i \sum_{\omega,\omega'} \Big\{ &\Gamma_i(-\omega')N(-\omega', T_i)[\hat{S}_i(\omega')\hat{\rho}_S(t)\hat{S}_i(\omega) - \hat{S}_i(\omega)\hat{S}_i(\omega')\hat{\rho}_S(t)] \\ &+ \Gamma_i(\omega)N(\omega, T_i)[\hat{S}_i(\omega')\hat{\rho}_S(t)\hat{S}_i(\omega) - \hat{\rho}_S(t)\hat{S}_i(\omega)\hat{S}_i(\omega')] \\ &+ \Gamma_i(\omega)[N(\omega, T_i)+1]\,[\hat{S}_i(\omega)\hat{\rho}_S(t)\hat{S}_i(\omega') - \hat{S}_i(\omega')\hat{S}_i(\omega)\hat{\rho}_S(t)] \\ &+ \Gamma_i(-\omega')[N(-\omega', T_i)+1][\hat{S}_i(\omega)\hat{\rho}_S(t)\hat{S}_i(\omega') - \hat{\rho}_S(t)\hat{S}_i(\omega')\hat{S}_i(\omega)]\Big\}\,,\end{aligned} \tag{A.19}$$

the damping rates $\Gamma_i(\omega)$ are frequency dependent through the environment density of states, which is non-zero only for ω greater than zero and the same goes for the mean number of thermal photons. The summation involves exclusively $\omega, \omega' > 0$ by exploiting Eq. (2.18), Eq. (2.19) and Eq. (2.20), so Eq. (A.19) becomes [18]

$$\begin{aligned}
\mathcal{L}_g\,\hat{\rho}_S = \frac{1}{2}\sum_i \sum_{(\omega,\omega')>0} \Big\{ & \Gamma_i(\omega')N(\omega',T_i)[\hat{S}_i^{(-)}(\omega')\hat{\rho}_S(t)\hat{S}_i^{(+)}(\omega)+ \\
& - \hat{S}_i^{(+)}(\omega)\hat{S}_i^{(-)}(\omega')\hat{\rho}_S(t)] + \Gamma_i(\omega)N(\omega,T_i)[\hat{S}_i^{(-)}(\omega')\hat{\rho}_S(t)\hat{S}_i^{(+)}(\omega)+ \\
& - \hat{\rho}_S(t)\hat{S}_i^{(+)}(\omega)\hat{S}_i^{(-)}(\omega')] + \Gamma_i(\omega)[N(\omega,T_i)+1][\hat{S}_i^{(+)}(\omega)\hat{\rho}_S(t)\hat{S}_i^{(-)}(\omega')+ \\
& - \hat{S}_i^{(-)}(\omega')\hat{S}_i^{(+)}(\omega)\hat{\rho}_S(t)] + \Gamma_i(\omega')[N(\omega',T_i)+1][\hat{S}_i^{(+)}(\omega)\hat{\rho}_S(t)\hat{S}_i^{(-)}(\omega')+ \\
& - \hat{\rho}_S(t)\hat{S}_i^{(-)}(\omega')\hat{S}_i^{(+)}(\omega)] + \Gamma_i(\omega')N(\omega',T_i)[\hat{S}_i^{(-)}(\omega')\hat{\rho}_S(t)\hat{S}_i^{(-)}(\omega)+ \\
& - \hat{S}_i^{(-)}(\omega)\hat{S}_i^{(-)}(\omega')\hat{\rho}_S(t)] + \Gamma_i(\omega')[N(\omega',T_i)+1][\hat{S}_i^{(-)}(\omega)\hat{\rho}_S(t)\hat{S}_i^{(-)}(\omega')+ \\
& - \hat{\rho}_S(t)\hat{S}_i^{(-)}(\omega')\hat{S}_i^{(-)}(\omega)] + \Gamma_i(\omega)N(\omega,T_i)[\hat{S}_i^{(+)}(\omega')\hat{\rho}_S(t)\hat{S}_i^{(+)}(\omega)+ \\
& - \hat{\rho}_S(t)\hat{S}_i^{(+)}(\omega)\hat{S}_i^{(+)}(\omega')] + \Gamma_i(\omega)[N(\omega,T_i)+1][\hat{S}_i^{(+)}(\omega)\hat{\rho}_S(t)\hat{S}_i^{(+)}(\omega')+ \\
& - \hat{S}_i^{(+)}(\omega')\hat{S}_i^{(+)}(\omega)\hat{\rho}_S(t)]\Gamma_i(\omega')N(\omega',T_i)[\hat{S}_i^{(-)}(\omega')\hat{\rho}_S(t)\hat{S}_i^{(0)}+ \\
& - \hat{S}_i^{(0)}\hat{S}_i^{(-)}(\omega')\hat{\rho}_S(t)] + \Gamma_i(\omega')[N(\omega',T_i)+1][\hat{S}_i^{(0)}\hat{\rho}_S(t)\hat{S}_i^{(-)}(\omega')+ \\
& - \hat{\rho}_S(t)\hat{S}_i^{(-)}(\omega')\hat{S}_i^{(0)}] + \Gamma_i(\omega)N(\omega,T_i)[\hat{S}_i^{(0)}\hat{\rho}_S(t)\hat{S}_i^{(+)}(\omega)+ \\
& - \hat{\rho}_S(t)\hat{S}_i^{(+)}(\omega)\hat{S}_i^{(0)}] + \Gamma_i(\omega)[N(\omega,T_i)+1][\hat{S}_i^{(+)}(\omega)\hat{\rho}(t)\hat{S}_i^{(0)}+ \\
& - \hat{S}_i^{(0)}\hat{S}_i^{(+)}(\omega)\hat{\rho}_S(t)] + \Omega_i^{+}(T_i)[\hat{S}_i^{(0)}\hat{\rho}_S(t)\hat{S}_i^{(0)} - \hat{S}_i^{(0)}\hat{S}_i^{(0)}\hat{\rho}_S(t)]+ \\
& + \Omega_i'^{+}(T_i)[\hat{S}_i^{(0)}\hat{\rho}_S(t)\hat{S}_i^{(0)} - \hat{\rho}_S(t)\hat{S}_i^{(0)}\hat{S}_i^{(0)}] + \Omega_i^{-}(T_i)[\hat{S}_i^{(0)}\hat{\rho}_S(t)\hat{S}_i^{(0)}+ \\
& - \hat{\rho}_S(t)\hat{S}_i^{(0)}\hat{S}_i^{(0)}] + \Omega_i'^{-}(T_i)[\hat{S}_i^{(0)}\hat{\rho}_S(t)\hat{S}_i^{(0)} - \hat{S}_i^{(0)}\hat{S}_i^{(0)}\hat{\rho}_S(t)]\Big\}.
\end{aligned} \tag{A.20}$$

Damping rates are expressed as $\Gamma_i(\omega) = 2\pi\, g_i(\omega)\,|\alpha(\omega)|^2$. $\Omega_i'^{\pm}$ and $\Omega_i^{\pm}$ are related to pure dephasing:

$$\Omega_i'^{\pm}(T_i) = \int_0^{+\infty} ds \int_0^{+\infty} d\nu\, g_i(\nu)\,|\alpha(\nu)|^2\,[N(\nu,T_i)+1]\,e^{\pm i\nu\, s}\,, \tag{A.21}$$

$$\Omega_i^{\pm}(T_i) = \int_0^{+\infty} ds \int_0^{+\infty} d\nu\, g_i(\nu)\,|\alpha(\nu)|^2\,[N(\nu,T_i)+1]\,e^{\pm i\nu\, s}\,. \tag{A.22}$$

Appendix B

Methods

The figures of Chp. 3 were realized by means of simulations. First, we analyze **only** the key passages of the code. Then, other cases will be considered.
The code was implemented through the programming language *Julia*. To begin with:

```
using QuPhys
using PyPlot
```

the package *QuPhys*[1] is a versatile tool for carrying out different kinds of computational quantum mechanics tasks. *PyPlot*, which is a famous Python library, allows us to manage the graphical settings of the figures.
The system Hamiltonian (Eq. (1.37)) was defined as function of its parameters:

```
N_q = 2
N_r = 80
N_trunc = 20
a = kron(destroy(N_r), eye(N_q))
σz = kron(eye(N_r), sigmaz() )
σx = kron(eye(N_r), sigmax())
σy = kron(eye(N_r), sigmay())

function σx2(ϵ, Δ)
    ω0 = (ϵ^2 + Δ^2)^1/2
    return (ϵ/ω0 * σz - Δ/ω0 * σx)
```

[1] https://albertomercurio.github.io/QuPhys.jl/dev/

```
end

function H(ϵ, Δ , ωr, η )
    ω0 = (ϵ^2 + Δ^2)^1/2
    return ω0/2 * σz + ωr * a' * a +
    ωr * η * ( a + a') * σx2(ϵ, Δ)
end
```

N_r represents the dimension of the Fock space of the light. In theory, it should be infinite, we chose a truncation value of 80, which is more than necessary for our applications. Moreover, *kron* computes the Kronecker product of the two required objects.
Two-dimensional spectra were obtained as follows:

```
ηl =[0.05, 0.2, 0.3, 0.7]
for j in eachindex(ηl)
  η =ηl[j]
  Δ = 3.0
  ωr = 1

  γr = 1e-3 * ωr
  γq = 1e-3 * ωr
  Tr = 0
  Tq = 0.07 * ωr
  N_ϵ = 200
  N_ω = 10000
  ω_max = 7* ωr
  ϵv = range(0, 4, N_ϵ)
  ωv = range(0, ω_max, N_ω)
  tol = 1e-15
```

```
prog = Progress(N_ϵ, showspeed=true)
spect_cap = zeros(N_ω , N_ϵ)
Threads.@threads
for i in eachindex(ϵv)
ϵ = ϵv[i]

ω0 = (Δ^2 + ϵ^2)^1/2

H_op = H(ϵ, Δ , ωr,  η)
fields = [1im * (a'-a) , σx2(ϵ, Δ)]

E , U , L = liouvillian_generalized(H_op, fields,
[γr, γq], [ωr, ω0], [Tr , Tq], N_trunc =
N_trunc, tol=tol)

Xp = dense_to_sparse((U'*(1im * (a'-a))*U
[1:N_trunc, 1:N_trunc], tol))

Xp = QuantumObject(triu(Xp, 1))
ωl , spec_tmp = spectrum(L, ωv, Xp', Xp,

solver=ExponentialSeries(tol=tol))

spect_cap[:,i] .= spec_tmp
next!(prog)
end

spect_cap[findall(isnan, spect_cap)] .=

minimum(spect_cap[findall(!isnan, spect_cap)])


spect_cap[findall(==(0), spect_cap)] .=
```

```
minimum(@view(spect_cap[findall(!=(0), spect_cap)]))

prog = Progress(N_ϵ, showspeed=true)
spect_ind = zeros(N_ω , N_ϵ)
Threads.@threads
for i in eachindex(ϵv)
ϵ = ϵv[i]

ω0 = (Δ^2 + ϵ^2)^1/2

H_op = H(ϵ, Δ , ωr,  η)
fields = [a+a'-2* η*σx2(ϵ, Δ) , σx2(ϵ, Δ)]

E , U , L = liouvillian_generalized(H_op, fields,
[γr,γq],[ωr, ω0], [Tr , Tq ],
N_trunc = N_trunc, tol=tol)

Xp = dense_to_sparse((U'*(-ω0*2*η*(Δ/ω0)*σy+

1im*ωr*(-a+a'))*U)

[1:N_trunc, 1:N_trunc], tol)

Xp = QuantumObject(triu(Xp, 1))
ωl , spec_tmp = spectrum(L, ωv, Xp', Xp, solver=
ExponentialSeries(tol=tol))
spect_ind[:,i] .= spec_tmp
next!(prog)
end

spect_ind[findall(isnan, spect_ind)] .=
```

```
  minimum(spect_ind[findall(!isnan, spect_ind)])
  normalization = maximum(spect_cap)
  spect_ind = spect_ind ./normalization
  spect_cap = spect_cap ./normalization

  spect_ind[findall(==(0), spect_ind)] .=

  minimum(@view(spect_ind[findall(!=(0), spect_ind)]))
end
```

This algorithm generates diagrams like Fig. 3.6 and Fig. 3.5 through an iterative process for several values of η. We focus on the essential instructions.

```
E , U , L = liouvillian_generalized(H_op, fields,
[γr, γq], [ωr, ω0], [Tr , Tq], N_trunc =
N_trunc, tol=tol)
```

liouvillian_generalized is a function of QuPhys that gives as output the eigenvalues of system Hamiltonian and the matrix that diagonalizes it. Furthermore, the Liouvillian is computed according to Eq. (3.6), note that it is necessary to provide a list of operators, *fields*, characterizing the interaction with the reservoir; the pure dephasing terms were added.
Once the Liouvillian is attained, the function *triu* permits to select the positive frequency component of the operator, negative frequency terms are immediately derived by taking the complex conjugate of the positive part. In the end:

```
  ωl , spec_tmp = spectrum(L, ωv, Xp', Xp,
  solver=ExponentialSeries(tol=tol))
```

In order to work out emission spectra (Eq. (3.2)), it is helpful vectorizing the density matrix, so that the Liouvillian superoperator becomes a matrix, and selecting the steady state which is equal to the eigenstate of the Liouvillian corresponding to the zero eigenvalue; at last correlation functions and fast Fourier transform are easily obtained through well established functions.

B.1 Intermediate case

Now, we reproduce the same figures of Chp. 3 when $\eta = 0.2$.

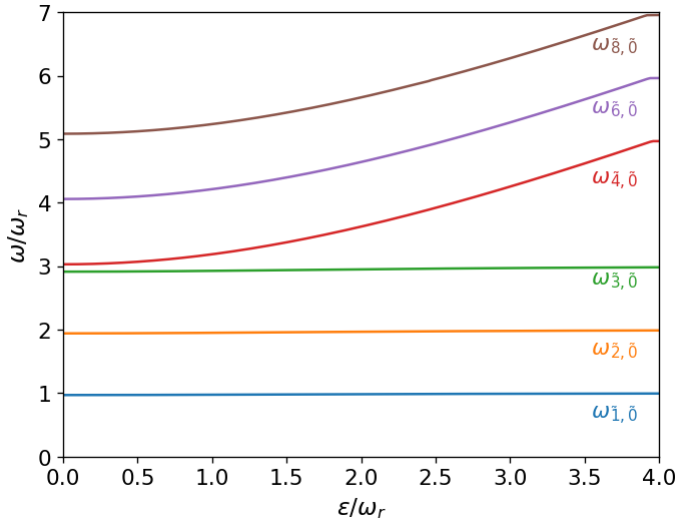

Figure B.1: **Energy level transitions for** $\eta = 0.2$. The figure shows the energy transitions, from several excited states, down to the ground state; they are indicated in the panel.

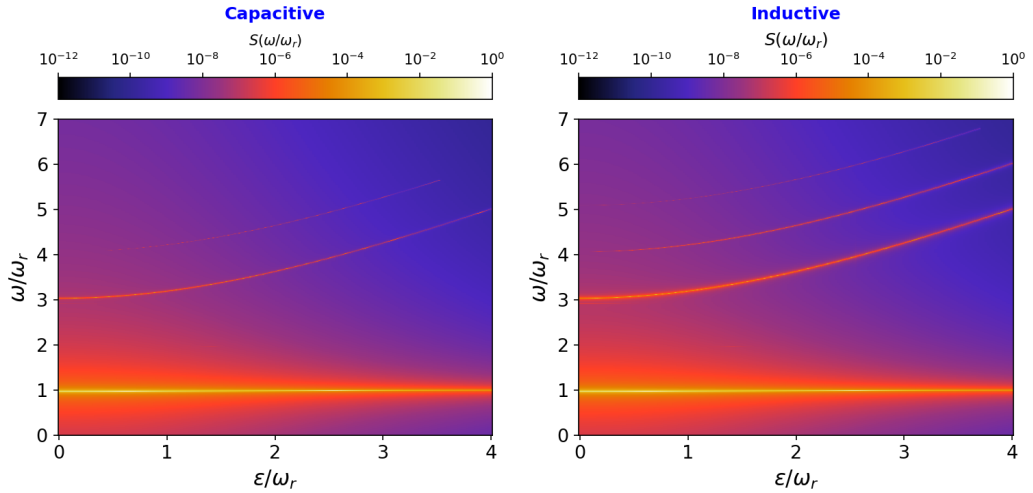

Figure B.2: **2-D emission spectra for** $\eta = 0.2$. It is obtained by numerically computing $S(\omega)$ (Eq. (3.2)) at the steady state. The spectrum lines are those of Fig. B.1.

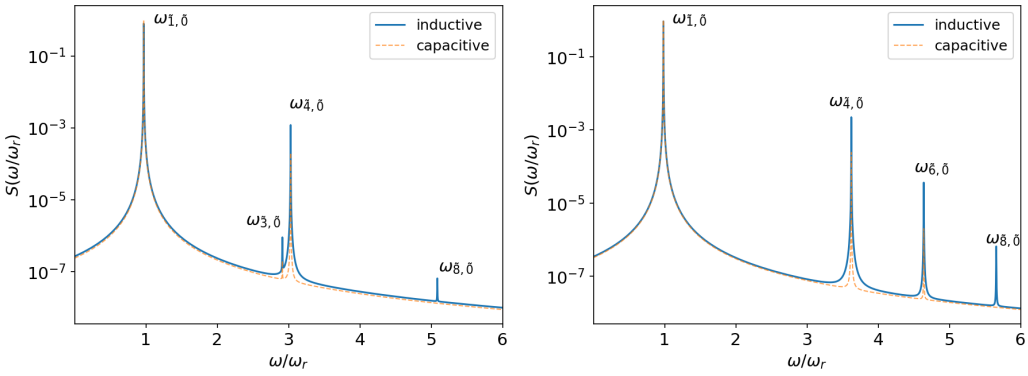

(a) (b)

Figure B.3: **1-dimensional emission spectra** for $\eta = 0.2$ and $T_q/\omega_r = 0.07$.
Panel **(a)** is made by fixing $\epsilon = 0$, while panel **(b)** for $\epsilon = 2$. The spectra were normalized with respect to the maximum value of the capacitive one; moreover, $S(\omega)$ is plotted on a logarithmic scale.

As shown by Fig. B.3, the pattern corresponds to what said in Sec. 3.2, although the discrepancies in the width of the "qubit-like" peaks, between the inductive and capacitive coupling, is less relevant compared to higher η ($\eta = 0.7$).

Bibliography

[1] J. P. Dowling and G. J. Milburn, "Quantum technology: the second quantum revolution," *Philosophical Transactions of the Royal Society of London. Series A: Mathematical, Physical and Engineering Sciences*, vol. 361, no. 1809, pp. 1655–1674, 2003.

[2] H.-L. Huang, D. Wu, D. Fan, and X. Zhu, "Superconducting quantum computing: a review," *Science China Information Sciences*, vol. 63, no. 8, p. 180501, 2020.

[3] A. Frisk Kockum, A. Miranowicz, S. De Liberato, S. Savasta, and F. Nori, "Ultrastrong coupling between light and matter," *Nature Reviews Physics*, vol. 1, no. 1, pp. 19–40, 2019.

[4] N. K. Langford, "Circuit qed - lecture notes," 2013.

[5] I. Georgescu and F. Nori, "Quantum technologies: an old new story," *Physics World*, vol. 25, no. 05, p. 16, 2012.

[6] C. Salter, R. Stevenson, I. Farrer, C. Nicoll, D. Ritchie, and A. Shields, "An entangled-light-emitting diode," *Nature*, vol. 465, no. 7298, pp. 594–597, 2010.

[7] C. Ciuti, G. Bastard, and I. Carusotto, "Quantum vacuum properties of the intersubband cavity polariton field," *Physical Review B*, vol. 72, no. 11, p. 115303, 2005.

[8] A. A. Anappara, S. De Liberato, A. Tredicucci, C. Ciuti, G. Biasiol, L. Sorba, and F. Beltram, "Signatures of the ultrastrong light-matter coupling regime," *Physical Review B*, vol. 79, no. 20, p. 201303, 2009.

[9] B. Zaks, D. Stehr, T.-A. Truong, P. M. Petroff, S. Hughes, and M. S. Sherwin, "Thz-driven quantum wells: Coulomb interactions and stark shifts in the ultrastrong coupling regime," *New Journal of Physics*, vol. 13, no. 8, p. 083009, 2011.

[10] S. Hughes, "Breakdown of the area theorem: carrier-wave rabi flopping of femtosecond optical pulses," *Physical review letters*, vol. 81, no. 16, p. 3363, 1998.

[11] O. Mücke, T. Tritschler, M. Wegener, U. Morgner, and F. Kärtner, "Signatures of carrier-wave rabi flopping in gaas," *Physical review letters*, vol. 87, no. 5, p. 057401, 2001.

[12] X. Gu, A. F. Kockum, A. Miranowicz, Y.-x. Liu, and F. Nori, "Microwave photonics with superconducting quantum circuits," *Physics Reports*, vol. 718, pp. 1–102, 2017.

[13] T. Niemczyk, F. Deppe, H. Huebl, E. Menzel, F. Hocke, M. Schwarz, J. Garcia-Ripoll, D. Zueco, T. Hümmer, E. Solano, *et al.*, "Circuit quantum electrodynamics in the ultrastrong-coupling regime," *Nature Physics*, vol. 6, no. 10, pp. 772–776, 2010.

[14] P. Forn-Díaz, J. Lisenfeld, D. Marcos, J. J. Garcia-Ripoll, E. Solano, C. Harmans, and J. Mooij, "Observation of the Bloch-Siegert shift in a qubit-oscillator system in the ultrastrong coupling regime," *Physical review letters*, vol. 105, no. 23, p. 237001, 2010.

[15] A. Settineri, O. D. Stefano, D. Zueco, S. Hughes, S. Savasta, and F. Nori, "Gauge freedom, quantum measurements, and time-dependent interactions in cavity QED," *Physical Review Research*, vol. 3, no. 2, 2021.

[16] F. Yoshihara, T. Fuse, S. Ashhab, K. Kakuyanagi, S. Saito, and K. Semba, "Superconducting qubit–oscillator circuit beyond the ultrastrong-coupling regime," *Nature Physics*, vol. 13, no. 1, pp. 44–47, 2017.

[17] F. Yoshihara, S. Ashhab, T. Fuse, M. Bamba, and K. Semba, "Hamiltonian of a flux qubit-LC oscillator circuit in the deep–strong-coupling regime," *Scientific Reports*, vol. 12, no. 1, p. 6764, 2022.

[18] A. Settineri, V. Macrí, A. Ridolfo, O. Di Stefano, A. F. Kockum, F. Nori, and S. Savasta, "Dissipation and thermal noise in hybrid quantum systems in the ultrastrong-coupling regime," *Phys. Rev. A*, vol. 98, p. 053834, 2018.

[19] H.-P. Breuer, F. Petruccione, *et al.*, *The theory of open quantum systems*. Oxford University Press on Demand, 2002.

[20] F. Beaudoin, J. M. Gambetta, and A. Blais, "Dissipation and ultrastrong coupling in circuit qed," *Phys. Rev. A*, vol. 84, p. 043832, 2011.

[21] U. Vool and M. Devoret, "Introduction to quantum electromagnetic circuits," *International Journal of Circuit Theory and Applications*, vol. 45, no. 7, pp. 897–934, 2017.

[22] M. H. Devoret, A. Wallraff, and J. M. Martinis, "Superconducting Qubits: A Short Review," *arXiv e-prints*, pp. cond–mat/0411174, 2004.

[23] S. M. Girvin, "113Circuit QED: superconducting qubits coupled to microwave photons," in *Quantum Machines: Measurement and Control of Engineered Quantum Systems: Lecture Notes of the Les Houches Summer School: Volume 96, July 2011*, Oxford University Press, 2014.

[24] J. Q. You and F. Nori, "Superconducting Circuits and Quantum Information," *Physics Today*, vol. 58, no. 11, pp. 42–47, 2005.

[25] S. Savasta, O. Di Stefano, A. Settineri, D. Zueco, S. Hughes, and F. Nori, "Gauge principle and gauge invariance in two-level systems," *Phys. Rev. A*, vol. 103, p. 053703, 2021.

[26] C. Cohen-Tannoudji, B. Diu, and F. Laloe, *Quantum Mechanics, Volume 1*, vol. 1. Wiley-VCH, 1986.

[27] P. Forn-Díaz, L. Lamata, E. Rico, J. Kono, and E. Solano, "Ultrastrong coupling regimes of light-matter interaction," *Rev. Mod. Phys.*, vol. 91, p. 025005, 2019.

[28] A. Stokes and A. Nazir, "Gauge ambiguities imply Jaynes-Cummings physics remains valid in ultrastrong coupling QED," *Nature Communications*, vol. 10, no. 1, p. 499, 2019.

[29] O. Di Stefano, A. Settineri, V. Macrì, L. Garziano, R. Stassi, S. Savasta, and F. Nori, "Resolution of gauge ambiguities in ultrastrong-coupling cavity quantum electrodynamics," *Nature Physics*, vol. 15, no. 8, pp. 803–808, 2019.

[30] P. Lambropoulos, *Fundamentals of quantum optics and quantum information*. Springer, 2007.

[31] J. Sakurai and J. Napolitano, *Modern Quantum Mechanics*. Cambridge University Press, 2017.

[32] A. Blais, A. L. Grimsmo, S. M. Girvin, and A. Wallraff, "Circuit quantum electrodynamics," *Rev. Mod. Phys.*, vol. 93, p. 025005, 2021.

[33] F. Mallet, F. R. Ong, A. Palacios-Laloy, F. Nguyen, P. Bertet, D. Vion, and D. Esteve, "Single-shot qubit readout in circuit quantum electrodynamics," *Nature Physics*, vol. 5, no. 11, pp. 791–795, 2009.

[34] L. Garziano, R. Stassi, V. Macrì, A. F. Kockum, S. Savasta, and F. Nori, "Multiphoton quantum rabi oscillations in ultrastrong cavity qed," *Phys. Rev. A*, vol. 92, p. 063830, 2015.

[35] C. Gardiner and P. Zoller, *Quantum noise: a handbook of Markovian and non-Markovian quantum stochastic methods with applications to quantum optics*. Springer Science & Business Media, 2004.

[36] A. Mercurio, V. Macrì, C. Gustin, S. Hughes, S. Savasta, and F. Nori, "Regimes of cavity qed under incoherent excitation: From weak to deep strong coupling," *Phys. Rev. Res.*, vol. 4, p. 023048, 2022.